Underlying physical mechanisms of winter precipitation extremes over India's high mountain region

Article

Accepted Version

Underlying Physical Mechanisms of Winter Precipitation Extremes over India's High Mountain Region

S. Nischal[1], Raju Attada[1*], Kieran M. R. Hunt[2,3], Mathew Barlow[4]

[1]Department of Earth and Environmental Sciences, Indian Institute of Science Education and Research Mohali, Mohali, Punjab, India

[2]Department of Meteorology, University of Reading, UK

[3]National Centre for Atmospheric Science, University of Reading, UK

[4]Environmental, Earth & Atmospheric Sciences, University of Massachusetts Lowell, Lowell, MA, USA

Revision Submitted to

Quarterly Journal of the Royal Meteorological Society

***Corresponding author:**

Raju Attada

Department of Earth and Environmental Sciences,

Indian Institute of Science Education and Research Mohali, India.

Email: rajuattada@iisermohali.ac.in

Abstract

Extreme precipitation events (EPEs) are among the most pervasive weather hazards in the western Himalayan region (WHR), posing widespread damage to life, infrastructure, and agriculture. This study investigates the synoptic and large-scale characteristics linked to winter precipitation extremes over the WHR. EPEs are identified as events surpassing the 95^{th} percentile threshold. A composite analysis is employed using two reanalyses—ERA5 and IMDAA to elucidate the synoptic conditions conducive to EPEs. Our findings suggest that EPEs in the WHR are linked to an intensified subtropical westerly jet, characteristically shifted to south than normal. Enhanced kinetic energy in the upper troposphere, attributed to increased baroclinic instability, reinforces moisture convergence and strengthens synoptic scale circulation, triggering deep convection and supporting EPEs. Notably, the interplay of pronounced Rossby waves sinking over the region, coupled with regional orography, significantly modulates the intensity of western disturbances (WDs) during extremes. Employing clustering analysis, we observed that the strongest EPEs are linked to anomalous vorticity in the upper to middle troposphere, together with deep convection via highly strengthened WDs, suggesting a potential role of large-scale influences. Using Lagrangian method, we identify that Arabian Sea is primary moisture source for EPEs in WHR. We further delved into the role of large-scale connections and EPEs through quasi-resonant amplification (QRA) analysis in the WHR using ERA5 data. The findings unveil the association of QRA with notably magnified, quasi stationary mid-latitude planetary waves characterized by wavenumbers 6/7/8 (baroclinic waves), contributing to precipitation extremes. Remarkably, distinct fingerprints of meridional temperature gradients, indicative of QRA, are linked to EPEs. Furthermore, this investigation discerns distinctive QRA patterns associated with varying clusters of extreme event intensities. Overall, our results emphasize the crucial role of QRA in amplifying planetary waves and promoting extreme precipitation in the WHR, underscoring the vulnerability of the region to evolving climate conditions and providing insights into the underlying physical mechanisms.

Keywords: Extreme precipitation events, western disturbances, western Himalayas, baroclinic instability, Rossby waves, Quasi-resonant amplification

1. Introduction

The Western Himalayan region (WHR, Figure 1a) significantly influences the hydro-meteorological conditions and climate variability in north India and adjoining regions. The diverse and topographic landscape of the WHR encompasses forests, cultivated areas, wetlands, glaciers, and urbanized zones (Figure 1b). This further affects the land-atmospheric exchange processes and precipitation variability (e.g. Singh et al. 1995; Beniston 2003; Anders et al. 2006; Dimri 2012; Hunt et al. 2018a; Nischal et al. 2022). In winter (December to February; DJF), western disturbances (WDs) –extratropical synoptic weather systems, contribute to a significant amount of annual precipitation to the region (e.g. Hunt et al. 2018a; Nischal et al. 2022). Moving eastward along upper tropospheric sub-tropical westerlies, these synoptic-scale eddies gather moisture from the Arabian Sea and encounter the regional orography across the WHR (e.g. Madhura et al. 2015; Hunt et al. 2018a). This intensifies the WDs and results in heavy precipitation (Ramaswamy 1956).

Winter precipitation in the WHR sustains the crucial glacial mass equilibrium, influencing regional river discharge and streamflow (Hasson et al. 2014). Given the vulnerability to precipitation variability, any key fluctuations could severely impact regional freshwater availability downstream in this vital glacier-dependent watershed, in turn, affecting millions (e.g. Messerli et al. 2004). Moreover, changing climate hold profound implications for this ecosystem and winter precipitation patterns (Tewari et al. 2017; Hunt et al. 2020), including the anticipated increase in hydroclimatic variability, modified precipitation patterns and intensified extremes (Miller et al. 2012; Madhura et al. 2015; Krishnan et al. 2019). Additionally, the steep topography of the WHR increases its susceptibility to intense surface runoff during extreme precipitation events (EPEs), enhancing the risk of avalanches, landslides, and floods, thus, rendering the WHR as a high-risk zone (Bookhagen and Burbank 2010; Priya et al. 2016; Acharya et al. 2023). Numerous instances of EPEs over the WHR have illustrated massive losses through cloudbursts induced by terrain-locked deep convective systems in valleys, and flash floods triggered by extratropical disturbances (Dimri et al. 2017; Houze et al. 2017; Hunt et al. 2021).

Recent studies suggest a rise in the frequency and intensity of winter EPEs in the WHR (Madhura et al. 2015, Shekhar et al. 2017, Krishnan et al. 2019, Rao et al. 2021; Nischal et al. 2023). Some attributable factors include a warming climate (Ballesteros-Cánovas et al. 2018), growing prevalence of atmospheric rivers (Nayak et al. 2021) and, increased WD variability through enhanced upper-level baroclinicity (Madhura et al. 2015). However, empirical evidence

is insufficient to firmly establish a trend in WD frequency, suggesting potential changes in intensity. The disastrous impacts of EPEs extend to both natural and anthropogenic ecosystems, resulting in damage to life, infrastructure, crops, and power networks, sparking serious concerns about their impacts on human lives (Dimri et al. 2021; Sati and Kumar, 2022). For instance, Figure 1c (Disastrous Weather Events catalogue by India Meteorological Department) illustrates the human mortality rate linked to winter extreme snowfall events over the WHR since the 1980s. Goklany (2009) suggested improvement in monitoring, forecasting, and preparedness for these events to potentially lower mortality rates, as evident in recent years (see Figure 1c). Furthermore, a holistic understanding of the associated dynamics and thermodynamics of EPEs can improve the accuracy of early warning systems which eventually helps in effective risk mitigation. Winter precipitation over the WHR is modulated to a large extent by various localized, synoptic and large-scale meteorological processes including variations in the sub-tropical westerly jet and WD activity, as well as more localized features such as cloudbursts. While the precipitation extremes and their associated dynamics have been relatively well-documented for the summer monsoon season (Priya et al. 2016; Revadekar et al. 2016; Vellore et al. 2016; Hunt et al. 2018b; Aggarwal et al. 2022), winter precipitation extremes and their causal mechanisms have received comparatively less attention (Madhura et al. 2015; Hunt et al. 2018b; Krishnan et al., 2019). Additionally, most available literature focuses on case studies, highlighting location or event-specific EPEs (e.g. Norris et al. 2015), underscoring the importance of in-depth research to address the potential ramifications of winter EPEs.

Recent research has also emphasized the critical role of large-scale planetary atmospheric dynamics in characterizing such weather extremes. Studies conducted by Petoukhov et al. (2013), Coumou et al. (2014), and Mann et al. (2018) shed light on Quasi-Resonant Amplification (QRA), a phenomenon linked to climate change associated Arctic warming i.e. Arctic amplification (AA). QRA occurs when these quasi-stationary atmospheric waves become trapped in a latitudinal waveguide (turning points around 30°N and 45°N), creating a zonally directed waveguide for specific wave numbers. When the waveguide is (almost) circumglobal, wave energy is efficiently trapped and waves constructively interfere with the forcing, leading to resonance and the growth of trapped planetary waves that are excited by thermal or orographic forcing (Petoukhov et al. 2013). This phenomenon contributes to weakening/meandering of mid-latitude westerlies, enhancing the possibility of weather extremes. Francis and Vavrus (2012) found that rapid Arctic warming weakens the poleward thickness gradient, decelerating large-scale Rossby waves. This,

in conjunction with enhanced wave amplitudes and elongated meridional flow, contributes to more frequent atmospheric blocking patterns and mid-latitude weather extremes. Zonal wavenumbers 6-8 have been known to resonate and amplify during summer extremes (e.g. Petoukhov et al. 2013; Mann et al. 2018). However, the influence of QRA on winter extremes over WHR is not investigated yet. Additionally, it has been observed that the strength of AA is relatively stronger during winter (e.g. Cohen et al. 2014), thus emphasizing the possible influence of QRA occurrences.

In this work, we investigate the synoptic and large-scale characteristics, including dynamical, thermodynamic, and moisture convective processes, associated with winter precipitation extremes in the WHR using high-resolution climate datasets. Collaterally, the study also evaluates the potential of recently released high-resolution Indian Monsoon Data Assimilation and Analysis (IMDAA) reanalysis in capturing these extremes over the WHR as well as their underlying mechanisms. At the end, we analyze the QRA characteristics to understand the potential links between planetary scale waves (induced by AA) and winter EPEs. This sheds light on how high-latitude dynamics influence EPEs in the WHR. Such understanding of precipitation extremes over high mountain region and their associated physical mechanisms is crucial for interpreting climate-change scenarios of extremes.

2. Data and Methods

2.1. Data

The study of precipitation extremes over the WHR requires high-resolution datasets, as the complex and heterogeneous Himalayan orography results in substantial spatial variability of both mean and extreme precipitation (Andermann et al., 2011). Here, we conducted an analysis of winter (DJF) EPEs using multiple high-resolution gridded datasets from different sources over the WHR (27.5-37.5°N and 72.5-80.5°E, see Figure 1a), from 1979 to 2019 except for Integrated MultisatellitE Retrievals (V3) for Global Precipitation Measurement (GPM-IMERG) dataset which spans 2000 onwards. To obtain daily precipitation observations, we used the India Meteorological Department's (IMD) dataset, which is based on measurements from 6955 rain gauge stations spread throughout the Indian subcontinent, interpolated to a resolution of 0.25°×0.25° (Pai et al. 2014). Nevertheless, the density of stations in the WHR is low. We also utilized the GPM-IMERG dataset, a high-resolution merged satellite product that combines microwave and infrared observations from the GPM satellite constellation with gauge observations

using the Day-1 IMERG algorithm (Huffman et al. 2015). IMERG is available from 2000 onwards at half-hourly temporal and 0.1° spatial resolution. The satellite product has been incorporated, as previous studies have evaluated its performance for studying precipitation extremes over complex topographies (Liu et al. 2020; Nepal et al. 2021).

Additionally, we used a recently released regional reanalysis dataset, IMDAA, which has a high spatial resolution of 12 km and covers the South Asian domain. IMDAA was developed through a collaboration between the National Centre for Medium Range Weather Forecasting, the UK Met Office, and IMD, using a unified atmospheric model and the four-dimensional variational (4D-Var) data assimilation technique (Rani et al. 2021). The dataset provides better representation of orographic features due to its high resolution (Nischal et al. 2022). Lastly, we employed the state-of-the-art global reanalysis ERA5, developed by the European Centre for Medium Range Weather Forecasts (fifth generation), which has a resolution of 0.25°×0.25°. We also considered daily values of various meteorological variables from IMDAA and ERA5, such as air temperature, specific humidity, vorticity, and three-dimensional wind components, at different pressure levels. Additionally, ERA5 and IMDAA-based WD tracks from Nischal et al. (2022) were utilized to identify and filter out the WD centers during EPEs over the WHR. Daily averages of outgoing longwave radiation (OLR) data from KALPANA-1 satellite (0.25°×0.25°) for 2004-2019 have also been used.

2.2. Methodology

2.2.1. Composite analysis of extremes

A wide discrepancy in precipitation patterns is observed among different datasets over the WHR (Baudouin et al. 2020; Nischal et al. 2022). Thus, we focus on analyzing how different datasets depict precipitation extremes over the WHR. Considering that the selected datasets are generated with different input data and dissimilar developmental methods, a strong agreement between any two of them indicates they are likely to be close to reality (Baudouin et al. 2020; Nischal et al. 2022). We also explore the fidelity of the newly-developed high-resolution IMDAA reanalysis in representing WH precipitation extremes during the winter season. It is to be noted that high resolution (spatial and temporal) as well as comparatively long temporal coverage provides the possibility of relatively better depiction of precipitation extremes (Rani et al. 2021; Nischal et al. 2022). Additionally, its ability to simulate both small and large-scale atmospheric dynamics (as it

represents the complex interplay between topography and mountain meteorology) during winter (Nischal et al. 2022) and summer (Saini and Attada, 2023) precipitation is credible.

We have selected datasets from different sources with at least daily precipitation records and high spatial resolution (≤ 25 km) for the analysis. Extreme days are defined as those when the average regional (27.5°N-37.5°N and 72.5°E-80.5°E) precipitation exceeds the 95th percentile threshold (Fig. 2a). This threshold is calculated by considering the precipitation values (including zero precipitation) across all the grid points in the region during the investigation period. Conversely, we classify the remaining days as non-extreme days. We further examined the composites of different atmospheric variables for extreme minus non-extreme days in the ERA5 and IMDAA reanalysis, using IMD-identified (observation-based) days in ERA5 and IMDAA's own identified days. Due to its shorter time span, IMERG was exclusively utilized for analyzing precipitation characteristics and not for further composite analysis. Nonetheless, it is noteworthy that the identified extreme and non-extreme days in IMERG exhibit similarities to other datasets for the period 2000-2019.

2.1.2. k-means clustering algorithm

In this study, we also seek to identify distinct weather regimes associated with extreme precipitation over the WHR, for which we use *k*-means clustering. Neal et al. (2020) previously used a similar technique to identify different weather patterns over India. The *k*-means clustering algorithm (Hartigan and Wong, 1979) is an iterative unsupervised vector quantification algorithm that groups a given set of n-dimensional (vector) points into distinct non-overlapping clusters (*k*), based on nearest possible cluster centroid value. The algorithm uses the Euclidean distances of each point in the cluster to measure similarities between them. The cluster points are grouped such that the sum of square of the distances for each point to the cluster mean or centroid gets minimized. The objective function, *F*, that the k-means clustering algorithm seeks to minimize is defined thus:

$$F = \sum_{j=1}^{k} \sum_{i=1}^{n_j} \|x_{i,j} - \mu_j\|^2 \quad (1)$$

where $x_{i,j}$ is a point vector in cluster j and μ_j is the center of cluster j, having n_j points. Firstly, the algorithm initializes the k-cluster centers randomly and each x point vector is grouped to a certain cluster j based on the closest cluster centroid value. Following this, the centroid values are

recalculated according to the means of all assigned points in each cluster and the algorithm keeps iterating until convergence.

Three clusters were deemed to be most appropriate for this analysis, enough to explain a sufficient amount of the variance associated with precipitation extremes over the region (following Hunt et al. 2018a and heuristic 'elbow method' developed by Hardy, 1994). The clustering has been carried out over the region (72.5-80.5°E, 27.5-37.5°N) for the following variables: Geopotential Height (GPH), vertical velocity, Potential Vorticity (PV), divergence, and cloud cover fraction.

2.1.3. Lagrangian parcel tracking for Moisture sources

To identify possible moisture pathways associated with an EPE, we employed a Lagrangian parcel tracking approach developed by Hunt et al. (2018b). This involves decomposing the atmosphere above the event of interest into uniformly spaced parcels, which are subsequently backward-advected from the region of interest using ERA5 wind data. Following the determination of the start date, time, and location of interest, we extract the three-dimensional wind vector at this point. The parcels undergo back-advection with 20-minute integration time, by changing the signs of wind vector components using a set of spherical equations (see more details in Hunt et al. 2018b). Due to limited reanalysis resolution, the resulting point may lack precise data coordinates in space or time. To mitigate this, local reanalysis fields are recalculated for the correct time through cubic spline interpolation. Subsequently, we employ a tricubic method (Lekien and Marsden 2005) to estimate the wind vector at the desired location. This iterative process continues, returning to the initial step with updated time, location, and winds, persisting for the specified integration duration. Here, we have back-advected forty parcels, equally spaced between 925 and 500 hPa for 10 days using local, contemporaneous ERA-5 winds at hourly temporal scale.

3. Results and Discussion

3.1. Precipitation extremes

Figure 2(a) depicts the percentile distributions for daily precipitation exceeding the 80^{th} percentile in different datasets over the WHR. Each line on the figure corresponds to a distribution that encompasses all the grid points across the study region (approximately 1850 grids). To ensure a fair comparison, the datasets have been re-gridded to a common spatial resolution of 0.25°. The findings indicate that a substantial proportion of winter precipitation in the WHR is sourced from

events surpassing the 80th percentile. Despite some differences, precipitation distribution shows a consistent pattern across all datasets. IMERG tends to underestimate comparatively lower percentiles but performs better than ERA5 at higher percentiles. IMD and IMDAA are often quite similar to each other. Excessive precipitation, surpassing the 95th percentile, in such hilly terrains can contribute to increased regional runoff, potentially causing downstream floods that can subsequently impact the Rabi crops sown during winter (e.g. Haritashya et al. 2006; Arora et al. 2016). Thus, 95th percentile has been chosen as the threshold for categorizing precipitation extremes and non-extremes.

Figure 2b illustrates how the composited region-wide precipitation anomalies during extremes evolve over time in the WHR. The notable anomalies are detectable from day -6 to day -2, with a more pronounced and remarkable increase occurring from day-2 to day 0. Following day 0, the anomalies decline sharply until day +2. The entire life cycle of these EPEs generally lasts roughly 4-5 days; similar to lifecycle of WDs (see Dimri et al. 2016). The evolution structure appears to exhibit a slight asymmetry between the advancing and decaying stages, suggesting that comparatively more robust characteristics and mechanisms are evident during the growing phase (e.g. Xu et al. 2022). The advancing phase also appears to be slightly slower than the decay phase, which aligns with the observed asymmetric precipitation footprints associated with a WD. This suggests the significant impact of WD characteristics on the winter precipitation in the WHR. A substantial rise in precipitation amounts during extremes is observed over the region as demonstrated by different datasets. WDs, suggested to be primary baroclinic cyclonic storms, develop and intensify through the release of energy via the atmospheric baroclinic response and their interaction with WHR orography (Hunt et al. 2018a), potentially contributing to precipitation extremes. Therefore, we also explored the temporal evolution of the composited region-wide anomalies for baroclinic instability using the baroclinic instability criterion (C), based on vertical wind shear and potential temperature (Phillips, 1954) in the upper (200 hPa) and lower troposphere (700 hPa), following Madhura et al. (2015). The baroclinic instability criterion (C) is defined thus:

$$c = \frac{f^2(u_{200} - u_{700})\theta_{500}}{\beta g H(\theta_{200} - \theta_{700})} \quad (2)$$

Here, ‘f’ denotes the Coriolis parameter, ‘θ’ is potential temperature, ‘u’ refers to the zonal wind speed, ‘β’ is the meridional gradient of Coriolis parameter, ‘g’ is the acceleration due to gravity and H is vertical height (m) between the 200 and 700 hPa pressure levels.

The evolution structure demonstrates a rise of baroclinic instability in the region four days preceding the occurrence of extreme precipitation. This enhancement becomes notably pronounced two days prior to the event and reaches its peak intensity one day prior. As the extreme precipitation day approaches, there is a notable and very sharp decrease in the baroclinic instability in the region, which continues to diminish until the following day. These findings indicate that enhanced baroclinicity serves as a leading indicator for the occurrence of such extremes. This increase in baroclinic response of the atmosphere can contribute to intensification of WDs and result in enhanced precipitation, provided sufficient atmospheric moisture is available. The growing baroclinicity can possibly influence the vertical component of relative vorticity and cause intense convection in the moist middle and upper troposphere, ultimately contributing to precipitation extremes (e.g. Para et al. 2019).

Higher positive anomalies for precipitation amounts are observed in the geographical distribution of composited precipitation anomalies on day 0 for all four datasets (Figure 2c-f). The highest differences are evident along the WHR foothills, where the climatological precipitation maxima are situated (Nischal et al. 2022); however, diversity in precipitation patterns among different datasets is quite evident. Regarding the geographical distribution, IMDAA and ERA5 reanalyses exhibit close agreement, indicating heavy precipitation across the entire orographic band- specifically lower Himalayas and foothills. However, IMD places heavy precipitation more towards the north and northwest, while IMERG indicates it in the foothills and lower elevations. It is noteworthy that IMD encounters challenges due to the lack of weather stations, leading to estimates derived from downslope extrapolation (Kishore et al. 2016). Satellite-based microwave retrievals, on the other hand, often faces difficulties in accurately assessing precipitation over snow-covered areas and estimating cold season orographic precipitation (e.g. Derin et al. 2016). Generally, differences in data generation sources and development algorithms create such variabilities among datasets (Baudouin et al. 2020; Nischal et al. 2022). Nonetheless, it is clear that precipitation extremes induce widely distributed heavy precipitation over the region, and it is crucial to understand their physical mechanisms.

3.2. Possible Mechanisms

To better understand the physical processes for precipitation extremes in the WHR, a diagnosis of synoptic and large-scale characteristics was performed. Composite anomalies for extreme minus non-extreme days were analyzed to gain insight into the associated physical conditions.

3.2.1. Synoptic Characteristics

a) Geopotential height, potential vorticity and winds

GPH anomalies are distinctive signatures of deep synoptic cyclonic troughs (Cannon et al., 2014; 2015), also known as WDs. Increased variability in upper and middle tropospheric GPH is associated with increased winter WD activity and precipitation (e.g. Lang and Barros, 2004; Cannon et al., 2015). Here, we present the composite maps of upper (200 hPa) and mid-tropospheric (500 hPa) GPH anomalies for precipitation extremes minus non-extremes in ERA5 and IMDAA (Figure 3a-d). At both levels, there is a marked negative GPH anomaly, with a minimum situated just west of the WHR at roughly 34°N-68°E (200hPa). The troughs formed are considerably more intense at 200 hPa than in the mid-troposphere. IMDAA and ERA5 exhibit a consistence in trough placement. The locations of WD centers (20°–40°N, 60°–82°E) during EPEs in ERA5 and IMDAA reveals that the majority of these centers are situated west of the WHR, aligning with the trough placements in respective datasets (Figure 3a-b). Notably, both ERA5 and IMDAA exhibit a concentrated pattern for WD centers, although minor disparities can be observed in terms of the precise locations of these centers within the datasets.

Positive PV in the upper-level corresponds to cyclonic circulation, while negative values usually suggest anticyclonic circulation. Moreover, a prominent meridional gradient of upper-level PV can strengthen the background flow, facilitating the expansion of cyclonic circulations to lower levels too (Hoskins 1997; Hoskins et al. 2007; Attada et al. 2022). The upper-tropospheric (300hPa) PV composite anomalies, depicted in Figure 3(e-f), illustrate the presence of strong positive PV anomalies along the WHR, providing conditions that support moist convection. The reduced atmospheric stability through higher PV flux have been linked to initiation of enhanced convection through Rossby wave-breaking (Attada et al. 2022). In particular, the interaction of WDs and stronger PV can help in the growth of WDs through moist baroclinic instability via orographic interactions during extremes.

Further, we examined meridionally-averaged (27.5-37.5°N), zonally distributed vertical structures of composited GPH anomalies (Figure 4a-b). A robust pressure trough, slightly tilted eastwards, is evident across the western Himalayan longitudes, with a core at centered at about 300 hPa. Such strong negative GPH anomalies are indicative of intense synoptic trough formation and the strengthening of potent cyclonic disturbances, and the structure is consistent with that of strong WDs (Hunt et al. 2018a). The interaction between the vertically-tilted deep trough and

regional topography induces orographic lifting of the flow, further intensifying the WDs through moist baroclinic instability. This process leads to heavy precipitation over the region, provided sufficient moisture supply is available (Lang and Barros, 2004; Cannon et al. 2014; Baudouin et al. 2021). Furthermore, we analyzed the differences in vertical wind speed between extreme and non-extreme days using a vertical-longitudinal cross section (Figure 4c). A stronger ascent indicating increased deep convection during extremes is observed over the WHR, with a maximum at about 450 hPa, located over steep orography, underscoring the crucial contribution of orographic forcing to the moist flow. In general, advancing WDs are associated with a pronounced ascent at the forefront, followed by a large-scale descent in the rear (Hunt et al., 2018a). During EPEs, these ascent and descent patterns become more intense, underpinning the essential role played by intense WDs during such events.

As WDs are carried to the WHR along the subtropical jet, the latitudinal position of the jet in turn affects the location and interactivity of WDs with orography, thus affecting precipitation patterns and intensity over the region (Krishnan et al. 2019). Thus, we examined the latitude-pressure cross-sections of zonally averaged (72.5°-80.5°E) zonal wind (200 hPa) composites during extremes and non-extremes (Figure 4d-e). Both ERA5 and IMDAA composites show that during extremes, the subtropical jet intensifies and shifts further south from its mean position over the WHR in winter. This affects WD activity through enhanced atmospheric baroclinicity and reduced stability, favoring the development of precipitation extremes.

b) Cloud cover and outgoing longwave radiation (OLR)

Dimri (2013) reported that subzero temperatures on snow-covered surfaces during winter hinder convective activity necessary for deep cloud activity over the WHR. Consequently, migrating WDs account for the majority of cloud cover in the region (Hatwar et al. 2005; Madhura et al. 2015; Sankar et al. 2021). Figure 5a-d displays composite anomalies based on ERA5 and IMDAA data, revealing changes in TCC and OLR across the WHR, respectively. During extremes, TCC experiences a widespread increase of up to 48%, indicating intensified precipitation. Simultaneously, OLR values exhibit a regionwide decrease, peaking in the zone of maximum observed precipitation, indicating the presence of deeper convection and higher cloud tops. Similar patterns are evident for OLR in satellite dataset KALPANA-1 (Figure S1). As OLR exhibits a clear sky dependence on surface feedback during winter, these negative anomalies signify the influence of stronger WDs contributing to increased precipitation (Dimri 2013).

c) Transient eddy kinetic energy and baroclinic instability

The variability of the large-scale circulation over the WHR and surrounding regions is characterized by higher-frequency transient eddies (i.e. WDs), which largely grow through the conversion of available potential energy into kinetic energy via baroclinic instability (Pedlosky, 1972; Chang and Orlanski, 1993). We investigated the variations in 200 hPa eddy kinetic energy (EKE) in IMDAA and ERA5 to highlight the localized impacts of winter westerly wave activity and subsequent energy transformation/exchange processes in the atmosphere. EKE is commonly described as the kinetic energy associated with the time-varying component of the horizontal velocity field.

$$EKE = \frac{1}{2}(u'^2 + v'^2) \quad (3)$$

$$u = \underline{u} + u' \text{ and } v = \underline{v} + v'$$

where, u and v are horizontal velocity components, $u'$and v' denote time-varying velocity components whereas, $\underline{u}$ and $\underline{v}$ represent the time mean velocity components. As our focus in this study is towards understanding the role of kinetic energy associated with synoptic transient eddies in driving precipitation extremes over the WHR, a Lanczos filter of 2-10 days has been applied to the anomalies of horizontal velocity fields. Composite anomalies for EKE (Figure 6a-b) indicate the accumulation and availability of regions with positive and negative kinetic energy in the atmosphere, indicating a Rossby wave train pattern. Increased EKE over the WHR indicates the existence of strong WDs, as we have already seen. This increase in EKE provides evidence for the presence of intense WDs over the region. The interplay of these WDs with strong PV gradients potentially fuels their growth through moist baroclinic instability. This, in turn, intensifies convection and EKE, ultimately resulting in substantial contributions to heavy precipitation.

It is well established that the subtropical jet is associated with strong upper-atmospheric baroclinicity and a large meridional temperature gradient, which help in the growth and maintenance of WDs (Singh and Agnihotri, 1977). A baroclinically unstable environment over the WHR favors a further intensification of these WDs and can lead to heavy precipitation (Hunt et al. 2018a,b; Sankar et al. 2021; Rao et al. 2022). Here, we explored the baroclinic nature of the atmosphere during EPEs using the baroclinic instability criterion (C) described earlier (Equation 1). Figure 6(c-d) depicts the differences in mean baroclinic instability between composites of precipitation extremes and non-extremes. The anomalies depict a baroclinic wave train, with a

pronounced indication of baroclinic instability over the WHR. Baroclinic instability has been proposed as a potential mechanism for release of energy from available potential energy in the atmosphere, thereby aiding in the growth and intensification of WDs (e.g. Rao and Rao, 1971). Hence, the presence of positive anomalies over the WHR implies an increased baroclinic activity, which indicates a stronger WD activity in the area, leading to heavy precipitation (e.g. Madhura et al. 2015). Given that the wave train extends far - beyond the WHR in both ERA5 and IMDAA, this indicates potential links to large-scale phenomenon that might contribute to a consistent intensification of WDs during precipitation extremes.

d) Moisture Transport Dynamics

Baroclinic instability is the primary driver of WDs, but their intensity might not always correlate with the intensity of observed precipitation levels, as it is contingent on moisture availability. Some winter disturbances with strong winds and temperature fluctuations may result in less intense precipitation, while slower-moving, less intense baroclinic lows may carry moisture over long distances, causing more prolonged precipitation. Catastrophic EPEs sometimes involves a long preconditioning process, accumulating moisture advected from distant sources within a subsident non-precipitating environment (e.g. Turato et al. 2004). The moisture then gets released in a concentrated area, such as the WHR, with moisture flux convergence arising out of a sudden synoptic forcing consequent to baroclinic development and the concomitant role of local orography. Winter precipitation over the WHR is primarily contributed through moisture advection from the Arabian Sea with secondary contributions from the Mediterranean, Caspian, and Red Seas (Dimri et al., 2015; Barlow et al. 2005). Here, we investigate moisture supply to the WHR during precipitation extremes through the examination of composite anomalies for vertically integrated moisture transport (VIMT; kg $m^{-1}s^{-1}$).

$$VIMT = \frac{1}{g} \int_{surface}^{300} qV \, dP \quad (4)$$

where, q is specific humidity, V is the horizontal wind, and dp is the vertical incremental change in pressure.

The composited anomalies in moisture transport, computed from surface to 300 hPa in ERA5 and IMDAA reanalysis, utilize surface pressure as the lower boundary, offering a more robust approach, particularly in the context of the complex topography of the WHR. Our analysis highlights the Arabian Sea to be a major moisture supply source to these extremes, which is

consistent with the findings of Hunt et al. (2018b) using back trajectory analysis (Figure 7a-b). Furthermore, a correlation analysis of these daily VIMT anomalies with the frequency of precipitation extremes over the WHR exhibits a strong correlation for moisture transport from the Arabian Sea (Figure 7c-d). Notably, both ERA5 and IMDAA produced almost identical results for VIMT and correlation analysis, indicating our findings are robust. Examining lead/lag composites of VIMT anomalies unveils a moisture flow from distant westward sources up to 4-5 days prior the event. Subsequently, moisture contributions become more pronounced from relatively nearby sources, especially the Arabian Sea, as the event day approaches (Figure S3). This suggests that an increase in the synoptic variability of WD associated westerly moisture transport on daily timescales is an essential precursor of precipitation extremes. The dynamics of moisture contributions for different intensity extreme events is further discussed in section 3.2.2.

Further, we utilize a Lagrangian approach (discussed in section 2.1.3) to investigate the moisture sources for three intense extreme precipitation events observed over the WHR. The selected cases under examination occurred at the following locations and dates: (a) 32.25°N, 76.5°E, 12 Dec 2017; (b) 32.75°N, 75.75°E, 5 Feb 2013; and (c) 33.25°N, 74.75°E, 5 Dec 2006. For each case study, we computed forty parcel trajectories backward for 10 days using local, contemporaneous ERA-5 winds (one-hourly data) and examined specific humidity along the trajectories (Figure 8). The findings unveil that air parcels are dispersed across Europe and North Africa, extending into neighbouring moisture sources, ten days preceding the event. Predominantly, these parcels originate near the North Sea and the Mediterranean Sea and are subsequently transported as boundary layer parcels distributed over the Black Sea, Caspian Sea, and the Arabian Gulf. Notably, there is substantial mid-/lower-tropospheric convergence associated with the events, indicative of the passage of a WD. Examination of specific humidity profiles along these trajectories highlights a significant moisture contribution from distant sources such as the North Sea (part of North Atlantic Ocean), Mediterranean Sea, and Black Sea. However, a noteworthy proportion of moisture is observed to originate specifically from the Arabian Sea. Overall, it can be suggested that the temporal scales of moisture accumulation may vary significantly depending on the scale of the precipitating event, with sources of moisture ranging from more to less remote, leading to corresponding variations in the temporal scales for moisture advection.

3.2.2. Classification of Extremes: k-means clustering

An important aspect of our study is to attempt to categorize winter precipitation extremes over the WHR. Such classification can provide useful insights into the different types of driving dynamics for extremes, specifically the underlying synoptic and large-scale mechanisms. To achieve this, we have applied k-means clustering algorithm to various dynamic parameters over extreme days, following Hunt et al. (2018a). The parameters incorporated in our analysis are: GPH, vertical velocity, PV, divergence, and cloud cover fraction (72.5-80.5°E, 27.5-37.5°N). The first step is to construct a standardized distribution for each field by computing standardized anomalies at each grid point over the study region for the entire multi-level (1000-100 hPa) time series of the extreme precipitation days, since the given fields have different statistical distributions. The anomaly fields have been re-gridded vertically to produce voxels with equal volumes to maintain homogeneity and prevent overpopulating lower altitudes with higher level density. Before clustering, the multi-dimensional array values in the field are unraveled and then concatenated into a single vector. Cluster mean vectors are then obtained by running the algorithm on this single vector and we then reconstruct the original three-dimensional fields from these. Here, we have classified the precipitation extremes into three clusters.

The vertical structures of various dynamic field clusters constructed using ERA5 are presented in Figure 9. The columns separate different clusters, arranged in increasing order of GPH anomaly in the atmosphere. Type 1, 2 and 3 clusters are separated by intensity in all the clusters where type 1 shows the weakest intensity extremes and type 3 shows strongest types of extremes, though being least common among all clusters. Type 2 which shows the extremes associated with relatively intermediate intensity, compared to other two clusters, seem to be the most common class of extremes over the WHR. Crucially, all clusters are somewhat dynamically similar, implying the presence of a common dynamical source of precipitation (i.e. WDs).

The zonally distributed vertical structure of GPH anomalies in the type 1 cluster shows a very weak, though vertically tilted trough over the region of interest, with a minimum over 66°E. A deepening of the trough aligned with a slight eastward shift in the location of the depression minimum can be observed as we move from type 1 to type 3 clusters. The depressions in type 2 and 3 clusters are identical to those associated with the WDs over the region (Dimri and Chevuturi 2016; Hunt et al. 2018a). The differences in their magnitudes indicate the strength of the WD in type 3 extremes being associated with the much intense WDs than type 2. Vertical wind in all three

clusters shows ascent over the region followed by a descent to the west, a pattern that intensifies as we move from type 1 to type 3.

A prominent upper-level maximum for PV over the study region can be observed in type 2 (situated at about 200–250 hPa), and type 3 clusters (located at about 400 450 hPa), whereas it is almost non-existent in type 1. These structures in the upper troposphere have characteristics resembling those of baroclinic instabilities elsewhere in the atmosphere, and of WDs themselves (Molinari et al. 1995; Robinson, 1989; Hunt et al. 2018a). The maximum in PV along the elevated topography of the WHR in turn leads to orographic forcing (as we see in the vertical velocity composites), thus supporting intense precipitation over the region. The zonally distributed structures of divergence in the type 2 and 3 clusters are also baroclinic, as concluded earlier. The ascending and descent patterns observed earlier are favored with upper-level divergence (~200-250 hPa) ahead and convergence behind, identical to what we observe for a typical WD. These convergence patterns and pronounced ascent, on interaction with the regional orography, ensure favorable environment for triggering precipitation extremes. The patterns of cloud cover fractions confirm this inference as we observe highly intensified cloud cover over the WHR in type 2 and 3 clusters, whereas type 1 cluster again shows relatively weaker patterns.

Further, we have tried to understand how these dynamical classifications relate to the observed precipitation patterns during extremes over the region. The patterns for mean precipitation during the extreme days for each cluster has been presented in Figure 9(p-r). As expected, type 1 cluster is associated with small-scale precipitation with weaker intensity, mostly reaching up to 12-24 mm/day. Type 3 cluster provides evidence of widely distributed large-scale precipitation with strong intensity (24-36 mm/day), whereas type 2 shows an intermediate kind of response. Overall, it becomes clear that the type 2 and type 3 clusters show strong evidence of association with WD structures and may be related to intense and very intense WDs. Lead-lag composites of VIMT anomalies have been constructed to elucidate moisture contributions from their sources for various event types. The results reveal that type 1 events exhibit a relatively greater moisture flow from distant westward sources preceding the events, in contrast to type 2 and 3 events (Figure S4-S6). Additionally, more intense events display a notably higher moisture supply from relatively nearby sources, particularly the Arabian Sea, as the event day approaches. The substantial variations in precipitation magnitudes between type 2 and 3 clusters suggest the existence of additional factors, beyond the presence of robust WDs, that potentially contribute to

the enhancing the intensity of these WDs. Therefore, our subsequent investigation will concentrate on comprehending the large-scale attributes linked to EPEs across the WHR.

3.2.3. Large scale characteristics

a) Response of Rossby wave source to precipitation extremes

The role of large-scale circulation in producing precipitation extremes over north Indian region during winter has been suggested to be linked with co-existence of jet with an upper-tropospheric quasi-stationary Rossby wave train (e.g. Hunt et al. 2018b). During winter, upper-tropospheric convergence and strong vertical motion in the subtropics generate anomalous vorticity (Nie et al. 2019). This upper-level vorticity source, denoted as Rossby wave source (RWS), sets off Rossby wave trains which circulate the tropical heating to extratropical atmospheric circulation (Sardeshmukh and Hoskins, 1988; Nie et al. 2019). Here, we have investigated the patterns of these RWSs during precipitation extremes over the WHR and surrounding regions. The RWS function is defined thus:

$$\frac{\partial \zeta_a}{\partial t} - v_\psi . \nabla \zeta_a = -\zeta_a D - v\chi . \nabla \zeta_a \quad (5)$$

where, $-\zeta_a D$ denotes the vortex stretching (relates to local strong divergence), the second term on the left-hand side is the advection of vorticity gradient by rotational wind (caused by large-scale divergent flow), which is related to Rossby wave propagation. The two right-hand side terms are forcing terms, together comprising the RWS.

The examination of RWS composite anomalies for precipitation extremes (Figure 10a) indicates that the WHR experiences strong negative anomalies in RWS, while adjacent regions show weak RWS, an amplification of the climatological patterns as observed by Nie et al. (2019) for winter RWS over the region. This suggests that strong WDs – themselves Rossby wave-like features – are dissipating over the WHR. During winter, Rossby wave sinks generated over the WHR are associated with negative anomalies for vortex stretching and positive anomalies for advection of vorticity gradient (e.g. Shimizu and de Albuquerque, 2010; Nie et al. 2019). This implies that large-scale divergent flow is the primary factor responsible for the generation of wave sinks in this region (see Ding et al. 2023). The interplay of anomalous PV flux, possibly from higher latitudes, with WDs in the vicinity of the WHR helps to strengthen the WDs associated local vortices. This contributes to intensified low-pressure systems and extreme precipitation. Therefore, the interaction of large-scale planetary circulation patterns and WDs over the

519 orographic regimes of the WHR influences the wintertime precipitation intensities in this region.
520 Nonetheless, it is important to note that the western Himalayan topography has a significant
521 influence on the variability patterns related to these Rossby wave trains.

522 **b) Wave activity flux (WAF)**

523 Large-scale, quasi-stationary high amplitude anomalies in the atmosphere can contribute to
524 abnormal weather patterns by affecting migratory weather systems and meridional flow
525 exchanges. The release of energy as a stationary Rossby wave train by these anomalies can
526 potentially result in the formation of atmospheric blocking patterns, with converging WAF often
527 indicating the development of a blocking anticyclone. Thus, converging/diverging patterns in
528 WAF linked to stationary Rossby waves on a meandering zonal mean flow can aid in
529 comprehending the underlying dynamics governing the genesis of these large-scale circulation
530 anomalies (Takaya and Nakamura, 1997). Additionally, the zonally asymmetric mean flow aids
531 the growth of these anomalies by converting available potential energy to kinetic energy via
532 baroclinic instability processes. The meridional eddy fluxes of momentum and heat play a key role
533 in the maintenance and forcing of atmospheric flow, and the Eliassen-Palm (EP) flux can be used
534 as a diagnostic tool to study their interaction. The composites of zonally averaged EP flux during
535 extreme and non-extreme days have been examined (Fig. 10b-c). The propagation of Rossby wave
536 groups, resembling the time-averaged life cycle of nonlinear baroclinic waves (Simmons and
537 Hoskins, 1980; Hoskins, 1983), was observed to move upwards from the surface at lower levels
538 and turn equatorward above 400 hPa. This pattern of EP cross sections has been found to be linked
539 with northward PV flux at lower levels and southward PV flux with strong wind shear in the upper
540 troposphere. Significantly, the flux is much stronger during extreme days as compared to non-
541 extreme days, indicating a stronger baroclinicity during extreme events that facilitates the
542 development and sustenance of cyclonic systems. Furthermore, a deceleration of zonal wind is
543 observed over the mid-latitudinal troposphere, which is much stronger during extreme events (Fig.
544 10d-e; contours).

545 Stronger EP convergence is also noted over almost the entire troposphere from 20° N
546 towards the poles, with EP divergence on the poleward side at lower levels (Fig. 10d-e). This
547 convergence is primarily related to energy flux and indicates that waves tend to slow down the
548 zonal mean flow with zonal energy being transformed into wave energy (Smith et al. 2022). The
549 deceleration is found to be much more pronounced during extreme events, indicating a higher

baroclinicity with more decelerated and/or meandering jet, and more energy available to fuel the persistence of cyclonic systems. The weakening/deceleration of mid-latitude westerlies has been linked to Arctic-sea loss due to Arctic warming, indicating an increased risk of extreme weather events (Smith et al. 2022). This generates decelerated quasi-stationary wave patterns that point to the existence of atmospheric blocking patterns characterized by a robust zonal flow both to the north and south of the blocking systems, and a shift from a zonal to a meridional flow pattern during initialization and decaying stages. During extreme days between 0-90°E and 20-80°N, a seemingly omega type of blocking pattern emerges, featuring a three-point vortex system (tripole) with an anticyclonic point vortex (high) situated on the poleward side of two cyclonic point vortices (Fig. 11a). This three-point vortex system can become stationary and guide the equatorward movement of cold polar air masses when the speeds become equal with the prevailing mid-latitudinal westerly winds (Detring et al. 2020).

The upper-tropospheric (200 hPa) WAF introduced by Takaya and Nakamura (2001) can be employed to investigate the instantaneous propagation of both migratory and stationary quasi-geostrophic waves on a zonally asymmetric basic flow for precipitation extremes. This study focuses only on the horizontal components of the WAF (Fig. 11b), which is formulated using the stream function (ψ) and the horizontal components of the basic flow wind vector (U and V). A circumglobally propagating WAF appears to be strengthening from an anomalous RWS, linked to an omega blocking pattern situated over the North Pacific. The flux propagates towards the northeast, eventually passing over the central-eastern region of North America, the pattern being consistent with the Pacific/North American teleconnection (Berry 1995). Subsequently, the WAF splits, with one branch turning equatorward into the tropical Atlantic and other penetrating into northern latitudes towards Arctic region. The former branch of WAF follows a similar path to migrating WDs, growing stronger as it moves through Mediterranean region and propagates across Middle East, Iran, Iraq, Afghanistan, Pakistan, finally penetrating into the WHR. The latter branch weakens over the mid-Arctic Ocean but gains strength as it reaches the western parts of Eurasian continent, corresponding to the enhances stream function (Fig. 11b) and GPH anomalies (Fig. 11a), finally reaching the WHR. As demonstrated, EPEs over the WHR are notably influenced and amplified by both mid-latitude and higher latitude systems, implying the role of large-scale mechanisms.

c) Role of Quasi-resonant amplification

Atmospheric blocking patterns have been previously connected to longitudinally extended, slow or stationary quasi-stationary waves (QSW) in the atmosphere (Kautz et al. 2022). Quasi-resonant amplification (QRA), a specific type of QSW, is characterized by a double-peaked westerly jet profile with stronger westerlies in subtropical and subpolar regions and weaker ones in midlatitudes. A circumglobal jet profile with turning points at around 30°N and 45°N can efficiently guide and enhance waves with k=6/7/8, leading to resonance. When these trapped waves are excited by thermal or orographic forcing, they grow in amplitude. The waveguide condition depends on the zonal wave number k and the shape of the zonal mean zonal wind ($\bar{u}$) profile, linked to meridional temperature gradients in the lower troposphere through the thermal wind relationship (Petoukhov et al. 2013; Mann et al. 2018). Here, we investigated the previously unexplored association between QRA and winter EPEs in the WHR. Zonal wave number spectra for the meridional wind fields at 300 hPa over 30° to 45°N (Fig. 12a) depict the peak in amplitudes for wavenumbers 6-8 during extremes compared to climatology, indicating the favorable conditions for the QRA occurrence (Petoukhov et al. 2013, Coumou et al. 2014, and Mann et al. 2018). Moreover, we explore the zonal wave zonal mean spectra for three types of EPEs previously classified via cluster analysis (Fig. 12b). Type 1 events, characterized by weak intensity precipitation, show amplitudes related to wavenumber 6 exclusively. Type 2 events, characterized by intermediate precipitation intensity, exhibit maximum amplitudes for wavenumbers 6, followed by 7 and 8 equally. Finally, type 3 events, with the most intense precipitation, display maximum amplitudes for wavenumber 8, followed by 7 and then 6, suggesting a highly meandering wave pattern during such extreme precipitation events. Additionally, the presence of a smaller-scale structure can be inferred from this pattern, which, in turn, can contribute to intensified quasi-geostrophic uplift due to the larger vorticity gradients observed.

Fig. 12(c-e) illustrates the interannual variability for the amplitudes of monthly mean Fourier components of 300 hPa meridional winds during individual winter months associated with wave numbers k=6,7 and 8, averaged over the latitudinal range of 30-45°N using ERA5 data between 1979-2019. Linear regression (trend lines not shown in the plot) suggests moderate positive trend in most of the month-wise amplitudes in each category, except for January in wave numbers 7 and 8, which showed a slight negative trend. Based on 1.5 SD amplitudes, years depicting the possible QRA characteristics were identified. It is further noteworthy that nearly all the identified QRA years exhibit a notable increase in either intensity or frequency, or both, of

EPEs (Fig S2). These findings support the possible association between QRA phenomena and the magnitude or occurrence rate of such winter precipitation extremes over the WH. Further, the selected years were examined for QRA fingerprint behavior using 1000-hPa meridional temperature anomalies (Fig. 12f-h). In general, the QRA fingerprint pattern displays negative values in the subtropics, followed by a rise to neutral values around mid-latitudes, then a decline towards negative values through 50°N, and pronounced positive values again at higher subpolar latitudes (e.g. Mann et al 2018). The QRA fingerprints associated with wave number 6 months were slightly distorted for January and February but well depicted for December. For wave numbers 7 and 8, the identified years through 1.5SD amplitudes displayed a pronounced QRA fingerprint.

Further, we observed the double-peaked westerly jet profile using 300hPa zonally averaged (30-80°E) zonal winds for the selected years in each wave number type, in agreement with QRA characteristics, with stronger westerlies in subtropics as well as subpolar regions and, weaker westerlies in midlatitudes (Fig. 12i). Coumou et al. (2014) reported that the frequency of QRA-linked weather extremes has increased as a response to AA, which is driven by feedback mechanisms such as anthropogenic greenhouse warming and ice-albedo feedback. The amplified warming has a more profound effect on the polar boundary of the waveguide. Due to the thermal wind relationship between upper-level westerlies and lower tropospheric temperatures, this AA may reduce upper-level midlatitude westerlies ($\bar{u}$), increasing the likelihood of QRA occurrences. The findings in our study suggest that QRA characteristics affect atmospheric dynamics and jet propagation, ultimately impacting winter precipitation over the WHR by altering Rossby wave characteristics.

3.4 Exploring QRA associated EPEs: Case study

Lastly, we investigated three instances of extreme precipitation over the last two decades, which persisted for at least three consecutive days and exceeded the 95th percentile threshold each day individually and given, that they fall into QRA years (Fig. 13). Additionally, we investigated if these events were linked to QRA characteristics. It is worth noting that the selected years align with those identified through the Fourier transform series based on 1.5 SD (standard deviation) amplitudes. The selected case studies include extreme precipitation occurrences on 2-5 December 2006, 3-6 February 2013, and 10-12 December 2017. Figure 13 (a-i; shaded) shows the spatial distribution of precipitation anomalies before, during, and after the occurrence of EPEs over the

WHR. During the EPEs, widely distributed precipitation anomalies reaching up to 16 mm/day can be observed in certain regions, with little or no precipitation before and after the events. These heavy precipitation events are supported by presence of strong positive PV flux, which move away from the region as the event duration surpasses (Figure 13a-i; contours). The analysis of QRA characteristics associated with the events illustrates the presence of QRA fingerprint in all selected events, with the December 2017 events exhibiting the most pronounced fingerprint than the February 2013 event (Fig. 13j). This suggests that the meridional temperature profile has a substantial impact on the QRA fingerprint for these events, with Arctic-amplified warming projecting onto this latitudinal anomaly pattern. Moreover, the events were associated with a prominent wave 6/7/8 pattern in the zonal mean zonal wave spectra, with the December 2017 event having the strongest amplitudes and the February 2013 event having weaker amplitudes (Fig. 13k). The anomalies for 300hPa meridional winds also indicated the presence of wavenumber 6/7/8 patterns, implying a connection to QRA characteristics (Fig. 13l-n). Lastly, the events also depicted the presence of a double-peaked westerly jet profile associated with QRA, with the February 2013 event having the least pronounced profile (Fig. 13o). Overall, the findings suggest that the observed EPEs over the WHR are associated with QRA characteristics, which may be influenced by Arctic amplified warming.

4. Summary and Conclusion

Winter precipitation over the WHR is crucial for agricultural sustenance and recharging the western Himalayan glaciers. However, the projected rise in precipitation extremes with respect to climate change signal is a key matter of concern. Our study focuses on examining the associated synoptic and large-scale characteristics, including the impact of planetary scale dynamics, that contribute to extreme precipitation in the WHR. We aim to contribute to a much needed and deeper understanding of the fundamental physical mechanisms underlying these extremes. The key inferences from our study is as follows:

- The majority of winter precipitation in the WHR is sourced from higher percentiles, with a substantial contribution from EPEs, amplifying the region's susceptibility to precipitation-related hazards.
- During EPEs, the primary wave guide for WDs - the sub-tropical westerly jet - intensifies and shifts southward and helps in developing much stronger baroclinicity, consistent with

673 structures of strengthened WDs. This implies that synoptic dynamics play a key role in the
674 increased variability of precipitation patterns over the WHR. The influence of local
675 thermodynamics on precipitation intensification can be ascertained through the presence
676 of higher kinetic energy and deeper convective activity during these events.

677 ● The analysis of potential moisture sources through the Lagrangian approach reveals that
678 intense EPEs over the WHR are associated with diverse moisture sources, spanning from
679 the North Sea and Mediterranean Sea to the Arabian Sea. Besides the established westward
680 advection of moisture, our study underscores the pivotal role of the Arabian Sea as a
681 significant moisture source for intense precipitation extremes in the WHR. The observed
682 strong positive correlations between the frequency of precipitation extremes and moisture
683 transport from the Arabian Sea highlight its crucial influence on such EPEs. Overall, the
684 diverse moisture origins identified through our Lagrangian approach, emphasizes the
685 intricate interplay of regional and distant moisture sources (with potentially varying
686 temporal scales of transport) in shaping the dynamics of extreme precipitation over the
687 WHR.

688 ● The classification of different types of precipitation extremes carried out using k-means
689 clustering reveals that intense and very intense WDs are associated with heavy
690 precipitation observed over the region, supported by high anomalous vorticity and deeper
691 convection in the atmosphere.

692 ● Enhanced atmospheric instability during EPEs may be caused by the interplay of WDs with
693 strong positive PV fluxes, possibly from higher latitudes, in the upper troposphere. This
694 can help in further strengthening the WDs in these orographic regimes through moist
695 baroclinic instability processes. The large-scale divergent flow resulting from these
696 interactions can also potentially lead to the formation of Rossby wave sinks in the region,
697 indicating the influence of large-scale planetary circulation patterns.

698 ● Large-scale, quasi-stationary anomalies can contribute to extreme precipitation in the
699 WHR by decelerating the mean flow and generating blocking patterns that enhance the
700 meridional flow exchanges. Such a phenomenon can contribute to further intensification
701 of passing WDs over the WHR and lead to persistent extreme precipitation patterns.

- Climate change associated arctic amplification may have a pronounced influence on the intensities of winter precipitation over the WHR through the QRA mechanism. Changes in meridional temperature gradients affect upper tropospheric wind profiles via the thermal-wind relationship. Extreme meandering QSW patterns in the wavenumber range 6/7/8 demonstrate the role of planetary-scale dynamics in influencing precipitation intensity in the third pole's sub-regions (WHR), underscoring the influence of large-scale mechanisms.
- The newly developed high-resolution reanalysis, IMDAA, realistically represents the regional precipitation distribution, trends as well as dynamical and thermodynamic contributions for precipitation extremes over the region.

In summary, our analysis highlights the importance of planetary, synoptic, and mesoscale processes as crucial drivers of extreme precipitation in the WHR. We observed that synoptic-scale dynamics become stronger during these events, which is further bolstered by local thermodynamics and large-scale Rossby wave dynamics. These factors work together to create conditions that promote the formation of intense weather systems with deeper convection and increased precipitation.

Acknowledgments

Nischal S gratefully acknowledges the financial assistance from the Prime Minister's Research Fellowship (PMRF), Ministry of Education, Government of India. This research work was supported by the Science and Engineering Research Board, Department of Science and Technology, Government of India under the "Start-up Research Grant (SRG) scheme" (SRG/ 2020/001857). Authors gratefully acknowledge ECMWF reanalysis and IMDAA reanalysis from NCMRWF, Ministry of Earth Sciences, Government of India. Authors are thankful to the anonymous reviewers for their constructive feedback which helped improve the quality of this work.

Conflict of interest

The authors declare no conflict of interest.

References

Acharya, A., Steiner, J. F., Walizada, K. M., Zakir, Z. H., Ali, S., Caiserman, A., & Watanabe, T. (2023). Snow and ice avalanches in high mountain Asia–scientific, local and indigenous knowledge. *Natural Hazards and Earth System Sciences Discussions*, 1-35. 10.5194/nhess-2022-287.

Aggarwal, D., Attada, R., Shukla, K.K., Chakraborty, R., & Kunchala, R.K. (2022). Monsoon precipitation characteristics and extreme precipitation events over Northwest India using Indian high resolution regional reanalysis. *Atmospheric Research*, 267, 105993. https://doi.org/10.1016/j.atmosres.2021.105993.

Andermann, C., Bonnet, S., & Gloaguen, R. (2011). Evaluation of precipitation data sets along the Himalayan front. *Geochemistry, Geophysics, Geosystems*, 12(7).

Anders, A. M., Roe, G. H., Hallet, B., Montgomery, D. R., Finnegan, N. J., & Putkonen, J. (2006). Spatial patterns of precipitation and topography in the Himalaya. *Geological Society of America Special Papers*, 398, 39-53.

Arora, M., Kumar, R., Singh, R. D., Malhotra, J., & Kumar, N. (2016). Analysis of unusual meteorological conditions that led to recent floods in Bhagirathi Basin (Uttarakhand Himalayas). *Hydrological Sciences Journal*, 61(7), 1238-1243.

Attada, R., Dasari, H. P., Ghostine, R., Kondapalli, N. K., Kunchala, R. K., Luong, T. M., & Hoteit, I. (2022). Diagnostic evaluation of extreme winter rainfall events over the Arabian Peninsula using high-resolution weather research and forecasting simulations. *Meteorological Applications*, 29(5), e2095. https://doi.org/10.1002/met.2095.

Ballesteros-Cánovas, J. A., Trappmann, D., Madrigal-González, J., Eckert, N., & Stoffel, M. (2018). Climate warming enhances snow avalanche risk in the Western Himalayas. *Proceedings of the National Academy of Sciences*, 115(13), 3410-3415.

Banerjee, D., & Singh, C. (2023). On the solid and liquid precipitation characteristics over the North-West Himalayan region around the turn of the century. *Climate Dynamics*, 60(3-4), 959-980. https://doi.org/10.1007/s00382-022-06325-x.

Barlow, M., Wheeler, M., Lyon, B., & Cullen, H. (2005). Modulation of daily precipitation over southwest Asia by the Madden–Julian oscillation. *Monthly weather reviews*, 133(12), 3579-3594.

Baudouin, J. P., Herzog, M., & Petrie, C. A. (2020). Cross-validating precipitation datasets in the Indus River basin. *Hydrology and Earth System Sciences*, 24(1), 427-450.

Baudouin, J. P., Herzog, M., & Petrie, C. A. (2021). Synoptic processes of winter precipitation in the Upper Indus Basin. *Weather and Climate Dynamics*, 2(4), 1187-1207. 10.5194/wcd-2-1187-2021.

Beniston, M., Keller, F., Koffi, B., & Goyette, S. (2003). Estimates of snow accumulation and volume in the Swiss Alps under changing climatic conditions. *Theoretical and Applied Climatology*, 76(1-2), 125-140.

763 Berry, E. K. (1995). The Pacific/North American Teleconnection (PNA). *Journal of Climate*, 8(3), 609-
764 632.

765 Bookhagen, B., & Burbank, D. W. (2010). Toward a complete Himalayan hydrological budget:
766 Spatiotemporal distribution of snowmelt and rainfall and their impact on river discharge. *Journal*
767 *of Geophysical Research: Earth Surface*, 115(F3).

768 Cannon, F., Carvalho, L. M., Jones, C., & Bookhagen, B. (2014). Multi-annual variations in winter westerly
769 disturbance activity affecting the Himalaya. *Climate Dynamics*, 44, 441-455.

770 Cannon, F., Carvalho, L. M., Jones, C., & Norris, J. (2015). Winter westerly disturbance dynamics and
771 precipitation in the western Himalaya and Karakoram: a wave-tracking approach. *Theoretical and*
772 *Applied Climatology*, 125, 27-44.

773 Cannon, F., Carvalho, L., Jones, C., & Bookhagen, B. (2014). Multi-annual variations in winter westerly
774 disturbance activity affecting the Himalaya. *Climate dynamics*, 44(1), 441-455.

775 Chang, E. K., & Orlanski, I. (1993). On the dynamics of a storm track. *Journal of Atmospheric*
776 *Sciences*, 50(7), 999-1015.

777 Coumou, D., Petoukhov, V., Rahmstorf, S., Petri, S., & Schellnhuber, H. J. (2014). Quasi-resonant
778 circulation regimes and hemispheric synchronization of extreme weather in boreal
779 summer. *Proceedings of the National Academy of Sciences*, 111(34), 12331-12336.

780 Das, L., & Meher, J. K. (2019). Drivers of climate over the Western Himalayan region of India: A
781 review. *Earth-Science Reviews*, 198, 102935.

782 Derin, Y., Anagnostou, E., Berne, A. et al. (2016). Multiregional satellite precipitation products evaluation
783 over complex terrain. *Journal of Hydrometeorology*, 17(6), 1817-1836.

784 Detring, C., Müller, A., Schielicke, L., Névir, P., & Rust, H. W. (2020). Atmospheric blocking types:
785 Frequencies and transitions. *Weather and Climate Dynamics Discussions*, 2020, 1-33.
786 10.5194/wcd-2020-62.

787 Dimri, A. P. (2012). Wintertime land surface characteristics in climatic simulations over the western
788 Himalayas. *Journal of Earth System Science*, 121(2), 329-344.

789 Dimri, A. P. (2013). Interannual variability of Indian winter monsoon over the Western Himalayas. *Global*
790 *and Planetary Change*, 106, 39-50.

791 Dimri, A. P., & Chevuturi, A. (2016). Western disturbances-an Indian meteorological perspective.
792 *Springer*.

793 Dimri, A. P., Allen, S., Huggel, C., Mal, S. et al. (2021). Climate change, cryosphere and impacts in the
794 Indian Himalayan Region. *Current Science*, 120(5), 774-790.

795 Dimri, A. P., Chevuturi, A., Niyogi, D. et al. (2017). Cloudbursts in Indian Himalayas: a review. *Earth-*
796 *Science Reviews*, 168, 1-23.

797 Dimri, A. P., Yasunari, T., Kotlia, B. S., Mohanty, U. C., & Sikka, D. R. (2016). Indian winter monsoon:
798 Present and past. *Earth-Science Reviews*, 163, 297-322.

799 Ding, Y., Sun, X., Li, Q., & Song, Y. (2023). Interdecadal Variation in Rossby Wave Source over the
800 Tibetan Plateau and its Impact on the East Asia Circulation Pattern during Boreal Summer.
801 *Atmosphere*, 14(3), 541.

802 Francis, J. A., & Vavrus, S. J. (2012). Evidence linking Arctic amplification to extreme weather in mid-
803 latitudes. *Geophysical Research Letters*, 39(6).

804 Goklany, I. M. (2009). Deaths and death rates from extreme weather events: 1900-2008. *Global Trends*,
805 13, 14.

806 Hardy A. 1994. An examination of procedures for determining the number of clusters in a data set. In New
807 Approaches in Classification and Data Analysis, Diday E, Lechevallier Y, Schader M, Bertrand P,
808 Burtschy B. (eds.): 178–185. *Studies in Classification, Data Analysis, and Knowledge*
809 *Organization. Springer*: Berlin, Heidelberg.

810 Haritashya, U. K., Singh, P., Kumar, N., & Singh, Y. (2006). Hydrological importance of an unusual hazard
811 in a mountainous basin: flood and landslide. *Hydrological Processes: An International Journal*,
812 20(14), 3147-3154.

813 Hartigan, J. A., & Wong, M. A. (1979). A k-means clustering algorithm. *Applied statistics*, 28(1), 100-108.

814 Hasson, S., Lucarini, V., Khan, M. R., Petitta, M., Bolch, T., & Gioli, G. (2014). Early 21st-century snow
815 cover state over the western river basins of the Indus River system. *Hydrology and Earth System*
816 *Sciences*, 18(10), 4077-4100.

817 Hatwar, H. R., Yadav, B. P., & Rao, Y. R. (2005). Prediction of western disturbances and associated
818 weather over Western Himalayas. *Current Science*, 88(7), 913-920.

819 Hoskins, B. (1997). A potential vorticity view of synoptic development. *Meteorological Applications*, 4(4),
820 325–334.

821 Hoskins, B. J., James, I. N., & White, G. H. (1983). The shape, propagation and mean-flow interaction of
822 large-scale weather systems. *Journal of Atmospheric Sciences*, 40(7), 1595-1612.

823 Hoskins, B. J., McIntyre, M. E., & Robertson, A. W. (2007). On the use and significance of isentropic
824 potential vorticity maps. *Quarterly Journal of the Royal Meteorological Society*, 133(625), 877–
825 946.

826 Houze Jr., R. A., McMurdie, L. A., Rasmussen, K. L., Kumar, A., & Chaplin, M. M. (2017). Multiscale
827 aspects of the storm producing the June 2013 flooding in Uttarakhand, India. *Monthly Weather*
828 *Reviews*, 145(11), 4447-4466.

829 Huffman, G. J., Bolvin, D. T., Braithwaite, D., Hsu, K., Joyce, R., Xie, P., & Yoo, S. H. (2015). NASA
830 global precipitation measurement (GPM) integrated multi-satellite retrievals for GPM (IMERG).
831 *Algorithm Theoretical Basis Document* (ATBD) Version, 4, 26.

832 Huffman, G. J., Bolvin, D. T., Nelkin, E. J. et al. (2007). The TRMM multisatellite precipitation analysis
833 (TMPA): Quasi-global, multiyear, combined-sensor precipitation estimates at fine scales. *Journal*
834 *of Hydrometeorology*, 8(1), 38-55.

835 Hunt, K. M. R., Turner, A. G., & Schiemann, R. K. H. (2021). How interactions between tropical
836 depressions and western disturbances affect heavy precipitation in South Asia. *Monthly Weather*
837 *Reviews.* 149(6), 1801-1825. 10.1175/MWR-D-20-0373.1.

838 Hunt, K. M. R., Turner, A. G., & Shaffrey, L. C. (2018a). The evolution, seasonality, and impacts of western
839 disturbances. *Quarterly Journal of the Royal Meteorological Society*, 144(710), 278-290.

840 Hunt, K. M. R., Turner, A. G., & Shaffrey, L. C. (2018b). Extreme daily rainfall in Pakistan and north India:
841 Scale interactions, mechanisms, and precursors. *Monthly Weather Review*, 146(4), 1005-1022.

842 Hunt, K. M. R., Turner, A. G., & Shaffrey, L. C. (2020). The impacts of climate change on the winter water
843 cycle of the western Himalaya. *Climate Dynamics.* 55, 2287–2307.

844 Hussain, S., Song, X., Ren, G., Hussain, I., Han, D., & Zaman, M. H. (2017). Evaluation of gridded
845 precipitation data in the Hindu Kush–Karakoram–Himalaya mountainous area. *Hydrological*
846 *Sciences Journal*, 62(14), 2393-2405.

847 Jain, S. K., Goswami, A., & Saraf, A. K. (2009). Role of elevation and aspect in snow distribution in
848 Western Himalaya. *Water Resources Management*, 23(1), 71-83.

849 Jingyu Liu, Juan Du, Yumeng Yang & Yini Wang (2020) Evaluating extreme precipitation estimations
850 based on the GPM IMERG products over the Yangtze River Basin, China, Geomatics, *Natural*
851 *Hazards and Risk*, 11:1, 601-618. 10.1080/19475705.2020.1734103.

852 Kalsi, S. R. (1980). On some aspects of interaction between middle latitude westerlies and monsoon
853 circulation. *Mausam*, 31(2), 305-308.

854 Kalsi, S. R., & Halder, S. R. (1992). Satellite observations of interaction between tropics and mid-latitudes.
855 *Mausam*, 43(1), 59-64.

Kautz, L. A., Martius, O., Pfahl, S., Pinto, J. G., Ramos, A. M., Sousa, P. M., & Woollings, T. (2022). Atmospheric blocking and weather extremes over the Euro-Atlantic sector–a review. *Weather and Climate Dynamics*, 3(1), 305-336. 10.5194/wcd-2021-56.

Kendall, M. G. (1975). Rank Correlation Methods. *Griffin*.

Kishore, P., Jyothi, S., Basha, G., Rao, S. V. B., Rajeevan, M., Velicogna, I., & Sutterley, T. C. (2016). Precipitation climatology over India: Validation with observations and reanalysis datasets and spatial trends. *Climate Dynamics*, 46, 541–556.

Kishore, P., Jyothi, S., Basha, G., Rao, S. V. B., Rajeevan, M., Velicogna, I., & Sutterley, T. C. (2016). Precipitation climatology over India: validation with observations and reanalysis datasets and spatial trends. *Climate dynamics*, 46, 541-556.

Krishnan, R., Sabin, T. P., Madhura, R. K. et al. (2019). Non-monsoonal precipitation response over the Western Himalayas to climate change. *Climate Dynamics*, 52(7), 4091-4109.

Lang, T. J., & Barros, A. P. (2004). Winter storms in the central Himalayas. *Journal of the Meteorological Society of Japan.* Ser. II, 82(3), 829-844.

Lekien, F., and J. Marsden, 2005: Tricubic interpolation in three dimensions. *J. Numer. Methods Eng*., 63, 455–471.

Madhura, R. K., Krishnan, R., Revadekar, J. V., Mujumdar, M., & Goswami, B. N. (2015). Changes in western disturbances over the Western Himalayas in a warming environment. *Climate Dynamics*, 44(3), 1157-1168.

Mann, H. B.: 1945, 'Nonparametric tests against trend', *Econometrica* 13, 245–259.

Mann, M. E., Rahmstorf, S., Kornhuber, K., Steinman, B. A., Miller, S. K., Petri, S., & Coumou, D. (2018). Projected changes in persistent extreme summer weather events: The role of quasi-resonant amplification. *Science advances*, 4(10), eaat3272.

Messerli, B., Viviroli, D., & Weingartner, R. (2004). Mountains of the world: vulnerable water towers for the 21st century. *Ambio*, 29-34.

Miller, J. D., Immerzeel, W. W., & Rees, G. (2012). Climate change impacts on glacier hydrology and river discharge in the Hindu Kush–Himalayas. *Mountain Research and Development*, 32(4), 461-467.

Molinari J., S. Skubis, and D. Vollaro, 1995: External influences on hurricane intensity. Part III: Potential vorticity evolution. *Journal of the Atmospheric Sciences*, 52, 3593–3606.

Narasimha Rao, N., Devi, U., Shekhar, M. S., & Singh, G. P. (2021). Trends of winter precipitation extremes over Northwest Himalaya. *Hydrological Sciences Journal*, 66(13), 1882-1891. https://doi.org/10.1080/02626667.2021.1969022.

Nayak, M. A., Azam, M. F., & Lyngwa, R. V. (2021). ERA5-based database of Atmospheric Rivers over Himalayas, *Earth System Science Data Discussions*. [preprint], https://doi.org/10.5194/essd-2020-397.

Neal, R., Robbins, J., Dankers, R., Mitra, A., Jayakumar, A., Rajagopal, E. N., & Adamson, G. (2020). Deriving optimal weather pattern definitions for the representation of precipitation variability over India. *International Journal of Climatology*, 40(1), 342-360. https://doi.org/10.1002/joc.6215.

Nepal, B., Shrestha, D., Sharma, S., Shrestha, M. S., Aryal, D., & Shrestha, N. (2021). Assessment of GPM-Era Satellite Products' (IMERG and GSMaP) Ability to Detect Precipitation Extremes over Mountainous Country Nepal. *Atmosphere*, 12(2), 254. https://doi.org/10.3390/rs12111836.

Nie, Y., Zhang, Y., Yang, X. Q., & Ren, H. L. (2019). Winter and summer Rossby wave sources in the CMIP5 models. *Earth and Space Science*, 6(10), 1831-1846.

Nischal, R., Attada, R., & Hunt, K. M. R. (2022). Evaluating Winter Precipitation over the Western Himalayas in a High-Resolution Indian Regional Reanalysis Using Multisource Climate Datasets. *Journal of Applied Meteorology and Climatology*, 61(11), 1613–1633. https://doi.org/10.1175/JAMC-D-21-0172.1.

Nischal, Rohtash K.S., Pathaikara A., Punde P., & Attada R. (2023). Hydrological Extremes in Western Himalayas-Trends and Their Physical Factors. *Natural Hazards - New Insights*. 10.5772/intechopen.109445.

Norris J., Carvalho L.M.V., Jones C., & Cannon F. (2015). WRF simulations of two extreme snowfall events associated with contrasting extratropical cyclones over the western and central Himalaya. *Journal of Geophysical Research: Atmospheres*, 120(8), 3114-3138.

Pai D.S., Rajeevan M., Sreejith O.P., Mukhopadhyay B., & Satbha N.S. (2014). Development of a new high spatial resolution (0.25×0.25) long period (1901-2010) daily gridded rainfall data set over India and its comparison with existing data sets over the region. *Mausam*, 65(1), 1-18.

Pedlosky, J. (1972). Finite-amplitude baroclinic wave packets. *Journal of Atmospheric Sciences*, 29(4), 680-686.

Petoukhov, V., Rahmstorf, S., Petri, S., & Schellnhuber, H. J. (2013). Quasiresonant amplification of planetary waves and recent Northern Hemisphere weather extremes. *Proceedings of the National Academy of Sciences of the United States of America*, 110(14), 5336–5341.

Phillips, N. A. (1954). Energy transformations and meridional circulations associated with simple baroclinic waves in a two-level, quasi-geostrophic model. *Tellus*, 6(3), 274-286.

Priya, P., Krishnan, R., Mujumdar, M., & Houze Jr., R. A. (2016). Changing monsoon and midlatitude circulation interactions over the Western Himalayas and possible links to occurrences of extreme precipitation. *Climate Dynamics*. 49, 2351–2364.

Ramaswamy C. (1956). On the sub-tropical jet stream and its role in the development of large-scale convection. *Tellus*, 8(1), 26-60.

Rani, S. I., Arulalan, T., George, J. P., Rajagopal, E. N. et al. (2021). IMDAA: High-Resolution Satellite-Era Reanalysis for the Indian Monsoon Region. *Journal of Climate,* 34(12), 5109-5133. https://doi.org/10.1029/2019JD030973.

Rao, V. B., & Rao, S. T. (1971). A theoretical and synoptic study of western disturbances. *Pure and Applied Geophysics,* 90(1), 193-208.

Revadekar, J.V., Varikoden, H., Preethi, B. et al. Precipitation extremes during Indian summer monsoon: role of cyclonic disturbances. *Natural Hazards*. 81, 1611–1625 (2016).

Robinson, W. A. (1989). On the structure of potential vorticity in baroclinic instability. Tellus A*: Dynamic Meteorology and Oceanography*, 41(4), 275-284.

Saini, R., & Attada, R. (2023). Analysis of Himalayan summer monsoon rainfall characteristics using Indian High-Resolution Regional Reanalysis. *International Journal of Climatology*. https://doi.org/10.1002/joc.8087.

Sankar, N. V., Babu, C. A., & Anil. (2021). Utility of INSAT 3D/3DR products in understanding the physical processes in clouds associated with western disturbance affecting North India during winter. *International Journal of Remote Sensing*, 42(22), 8440-8467. 10.1080/01431161.2021.1971791.

Sankar, N.V., Babu, C.A. (2020) Role of vorticity advection and thermal advection in the development of western disturbance during North Indian winter. *Meteorology and Atmospheric Physics,* 132, 515–529. https://doi.org/10.1007/s00703-019-00704-6.

Sardeshmukh, P. D., & Hoskins, B. J. (1988). The generation of global rotational flow by steady idealized tropical divergence. *Journal of the Atmospheric Sciences,* 45(7), 1228-1251.

Sati, V.P., Kumar, S. (2022). Environmental and economic impact of cloudburst-triggered debris flows and flash floods in Uttarakhand Himalaya: a case study. *Geoenviron Disasters,* 9, 5. https://doi.org/10.1186/s40677-022-00208-3.

Shekhar, M. S., Chand, H., Kumar, S., Srinivasan, K., & Ganju, A. (2010). Climate-change studies in the western Himalaya. *Annals of Glaciology*, 51(54), 105-112.

Shekhar, M. S., Rao, N. N., Paul, S., Bhan, S. C., Singh, G. P., & Singh, A. (2017). Winter precipitation climatology over Western Himalaya: Altitude and Range wise study. *The Journal of Indian Geophysical Union*, 21(2), 148-152.

Shimizu, M.H., de Albuquerque Cavalcanti, I.F (2011). Variability patterns of Rossby wave source. *Climate Dynamics* 37, 441–454.

Simmons, A. J., & Hoskins, B. J. (1980). Barotropic influences on the growth and decay of nonlinear baroclinic waves. *Journal of Atmospheric Sciences*, 37(8), 1679-1684.

Singh, M. S., & Agnihotri, C. L. (1977). Baroclinity over India in winter and its relation to western disturbances and jet streams-part I. *Mausam*, 28(3), 303-310.

Singh, P., Ramasastri, K. S., & Kumar, N. (1995). Topographical influence on precipitation distribution in different ranges of western Himalayas. *Hydrology Research*, 26(4-5), 259-284.

Smith, D.M., Eade, R., Andrews, M.B. et al. (2022). Robust but weak winter atmospheric circulation response to future Arctic-sea ice loss. *Nature Communications*, 13(1), 727. https://doi.org/10.1038/s41467-022-28283-y.

Takaya, K., & Nakamura, H. (1997). A formulation of a wave-activity flux for stationary Rossby waves on a zonally varying basic flow. *Geophysical Research Letters*, 24(23), 2985-2988.

Tewari, V.P., Verma, R.K. & von Gadow, K (2017). Climate change effects in the Western Himalayan ecosystems of India: evidence and strategies. *Forest Ecosystems*, 4, 13.

Turato, B., O. Reale, and F. Siccardi (2004), Water vapor sources of the October 2000 Piedmont flood. *Journal of Hydrometeorology*, 5, 693–712.

Vellore, R.K., Kaplan, M.L., Krishnan, R. et al. (2016). Monsoon-extratropical circulation interactions in Himalayan extreme rainfall. *Climate Dynamics*, 46(11), 3517–3546.

Webster, P. J., & Stephens, G. L. (1980). Tropical upper-tropospheric extended clouds: Inferences from winter MONEX. *Journal of Atmospheric Sciences*, 37(7), 1521-1541.

Xu, P., Wang, L., & Ming, J. (2022). Central Asian precipitation extremes affected by an intraseasonal planetary wave pattern. *Journal of Climate*, 35(8), 2603-2616. https://doi.org/10.1175/JCLI-D-21-0657.1.

Ye, B., Yang, D., Ding, Y., Han, T., & Koike, T. (2004). A bias-corrected precipitation climatology for China. *Journal of Hydrometeorology*, 5(6), 1147-1160.

List of Figures:

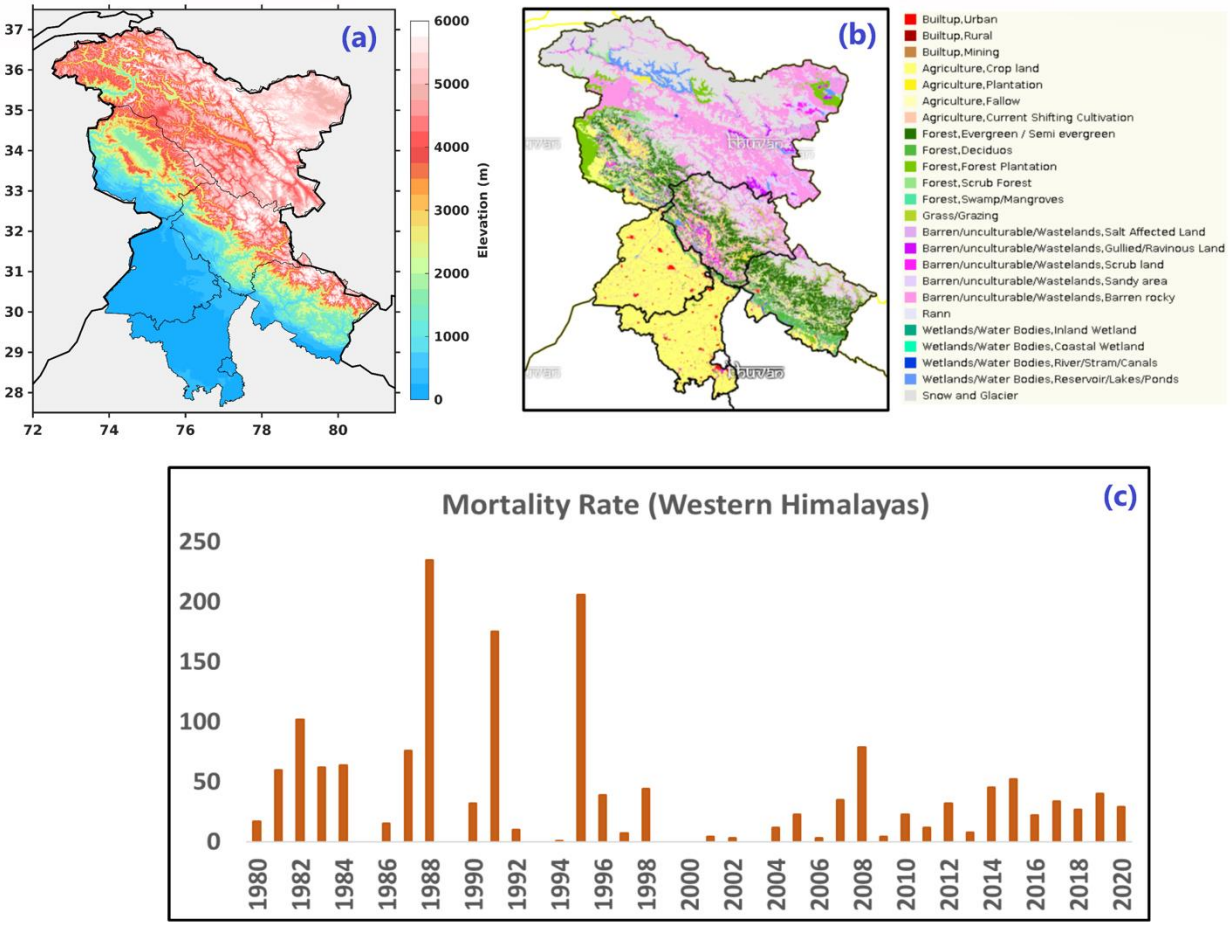

Figure 1: Topographic map of the western Himalayan region (WHR; a), Land Use Land Cover map (b) for the region from NRSC, Bhuvan (Indian Space Research Organisation). Figure 1c shows human mortality rate due to extreme snowfall events over the WHR during the winter season between 1980-2020.

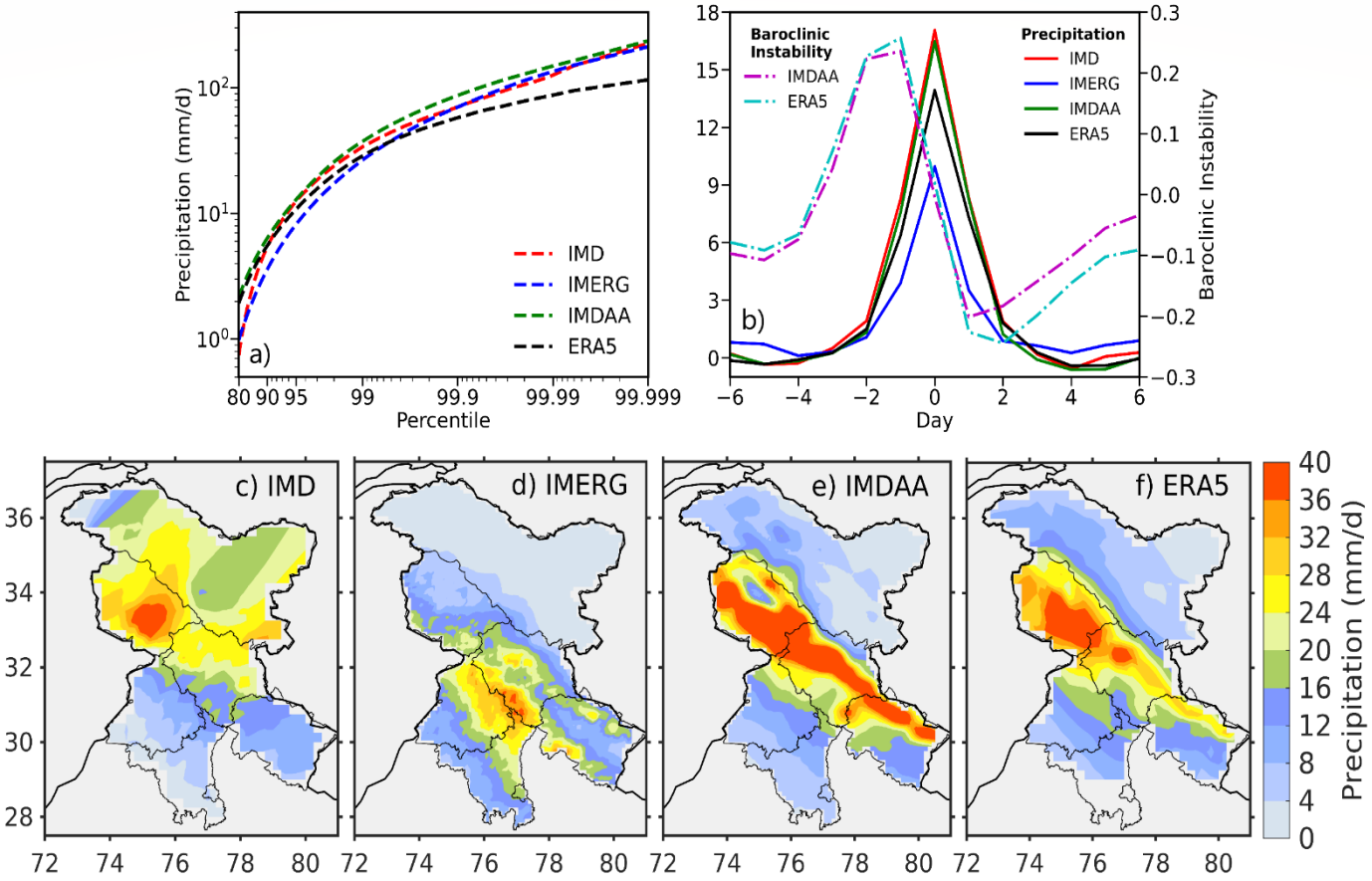

Figure 2: Percentile distribution of winter (DJF) Precipitation (unit: mm/day) in IMD, IMDAA and ERA5 datasets during 1979-2019 and from 2001-2019 in GPM-IMERG over the WHR (a), daily scale evolution of regionally averaged precipitation anomalies during extreme precipitation days (b; solid lines). Dashed lines in (b) represent the regionally averaged baroclinic instability index anomalies during precipitation extremes. (c-f) Spatial distribution of composite precipitation anomalies (precipitation observed during extreme days (exceeding 95th percentile) minus non-extreme days) for winter precipitation.

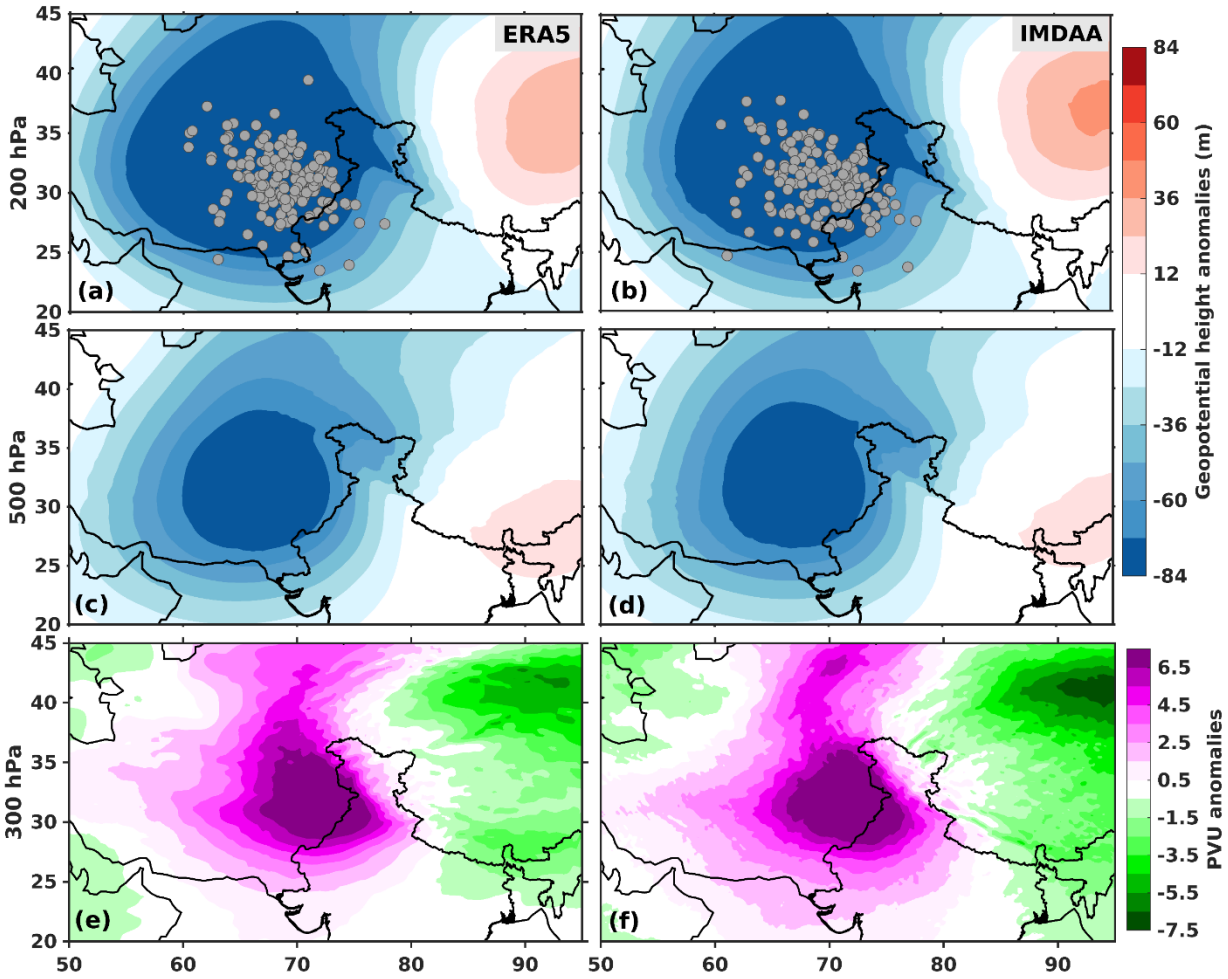

Figure 3: Composite anomalies (extremes minus non-extremes) for DJF geopotential height at 200 hPa (a-c, unit: m) and 500 hPa (b-d, unit: m) for the period 1979- 2019 and, 300 hPa baroclinic potential vorticity (e-f, unit: PVU). 1 PVU (potential vorticity units) here is equivalent to 10^{-6} $km^2/kg/s$. Western Disturbance centres during the extreme precipitation days has been represented using grey scatter points (a-b).

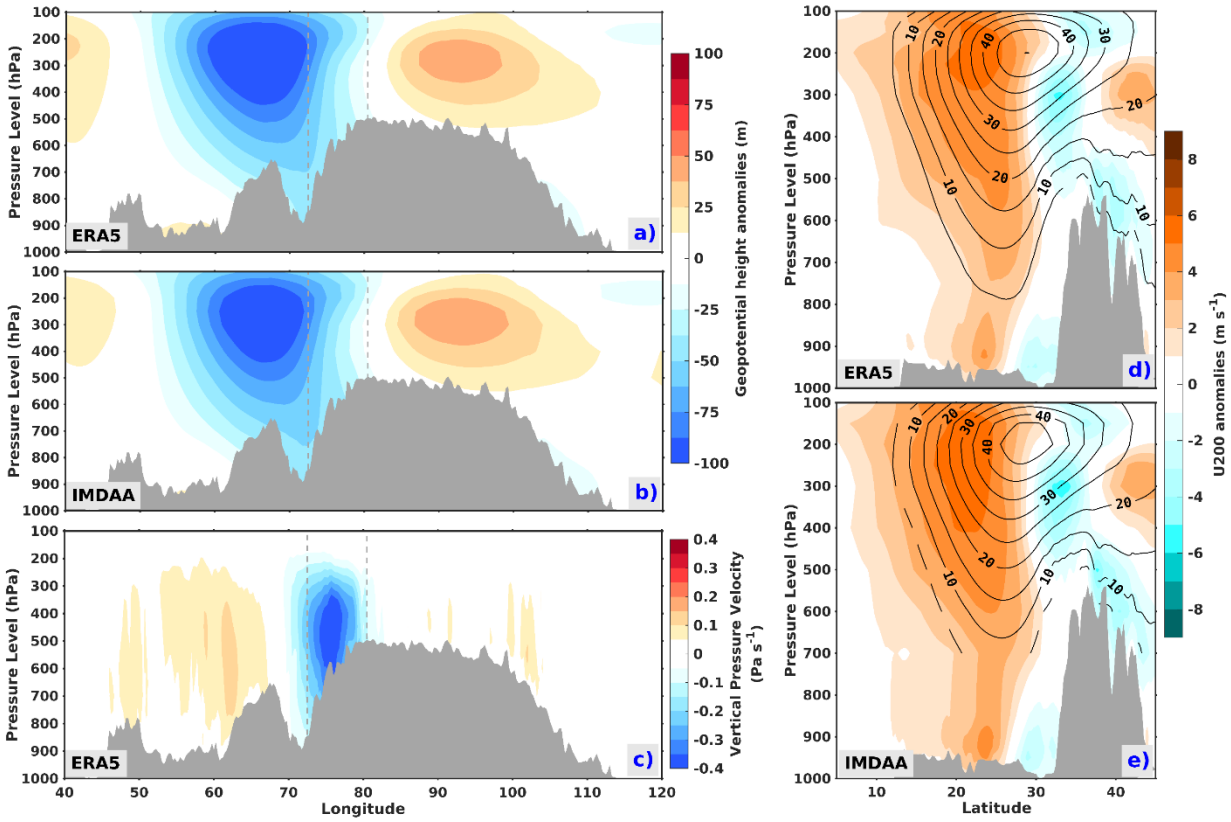

Figure 4: Vertical structure of DJF geopotential height composite anomalies (a-b, unit: m) averaged latitudinally over 27.5°-37.5°N in ERA5 and IMDAA respectively and, vertical velocity (c, unit: Pa/s) in ERA5 from 1979-2019. The longitudinal bounds of the study region have been represented by dashed lines in grey (a-c). The panels (d) and (e) show the vertical structures for composite anomalies of zonal wind (U200) speed during extremes (shaded, unit: m/s) and non-extremes (contours, unit: m/s). Grey areas indicate the presence of orography.

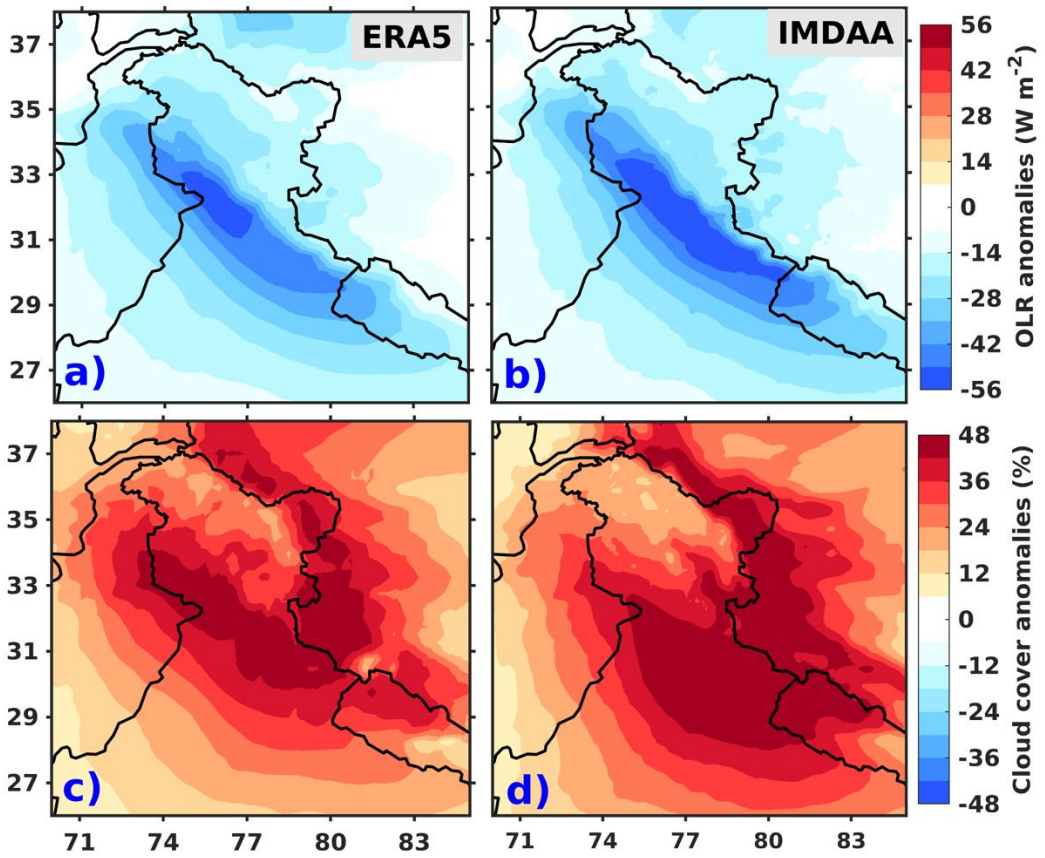

Figure 5: Composite anomalies (extremes minus non-extremes) for (a-b) total cloud cover (unit: %) and, (c-d) outgoing longwave radiation (OLR, unit: W/m^2) in ERA5 and IMDAA datasets from 1979-2019 during winter season (DJF).

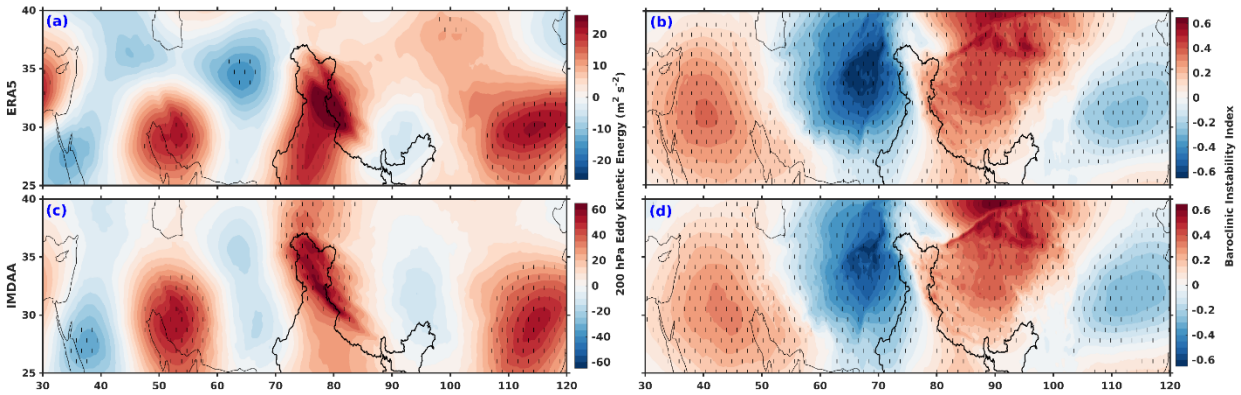

Figure 6: Wintertime composite anomalies for Eddy Kinetic Energy (a-b; unit: m^2s^{-2}) and, Baroclinic instability index (c-d) in ERA5 and IMDAA datasets during 1979- 2019.

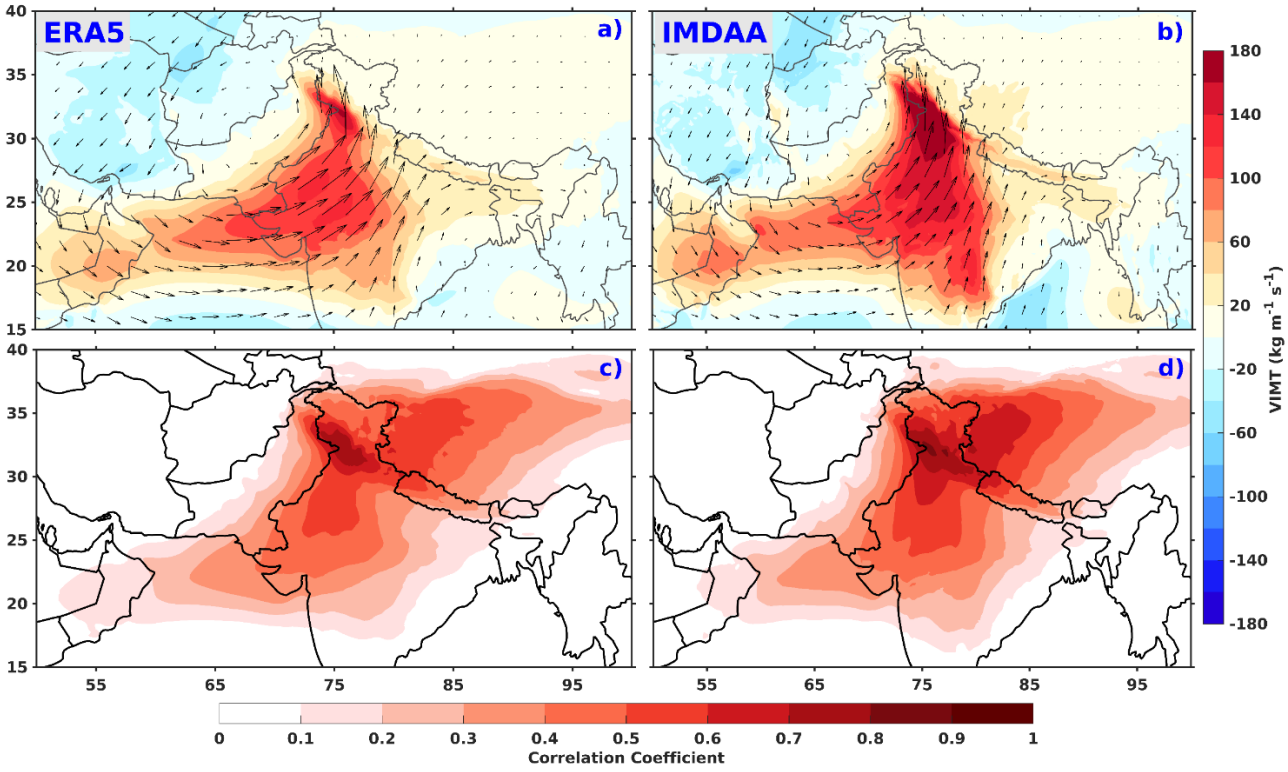

Figure 7: Composite anomalies (extremes minus non-extremes) for vertically integrated moisture transport (VIMT; shaded (magnitude) and vectors, unit: kg m^{-1} s^{-1}) between surface and 300 hPa and, correlation between VIMT and frequency of extremes exceeding 95th percentile over the box (72.5°E-80.5°E, 27.5°N-37.5°N) in ERA5 and IMDAA for 1979-2019 during the winter season.

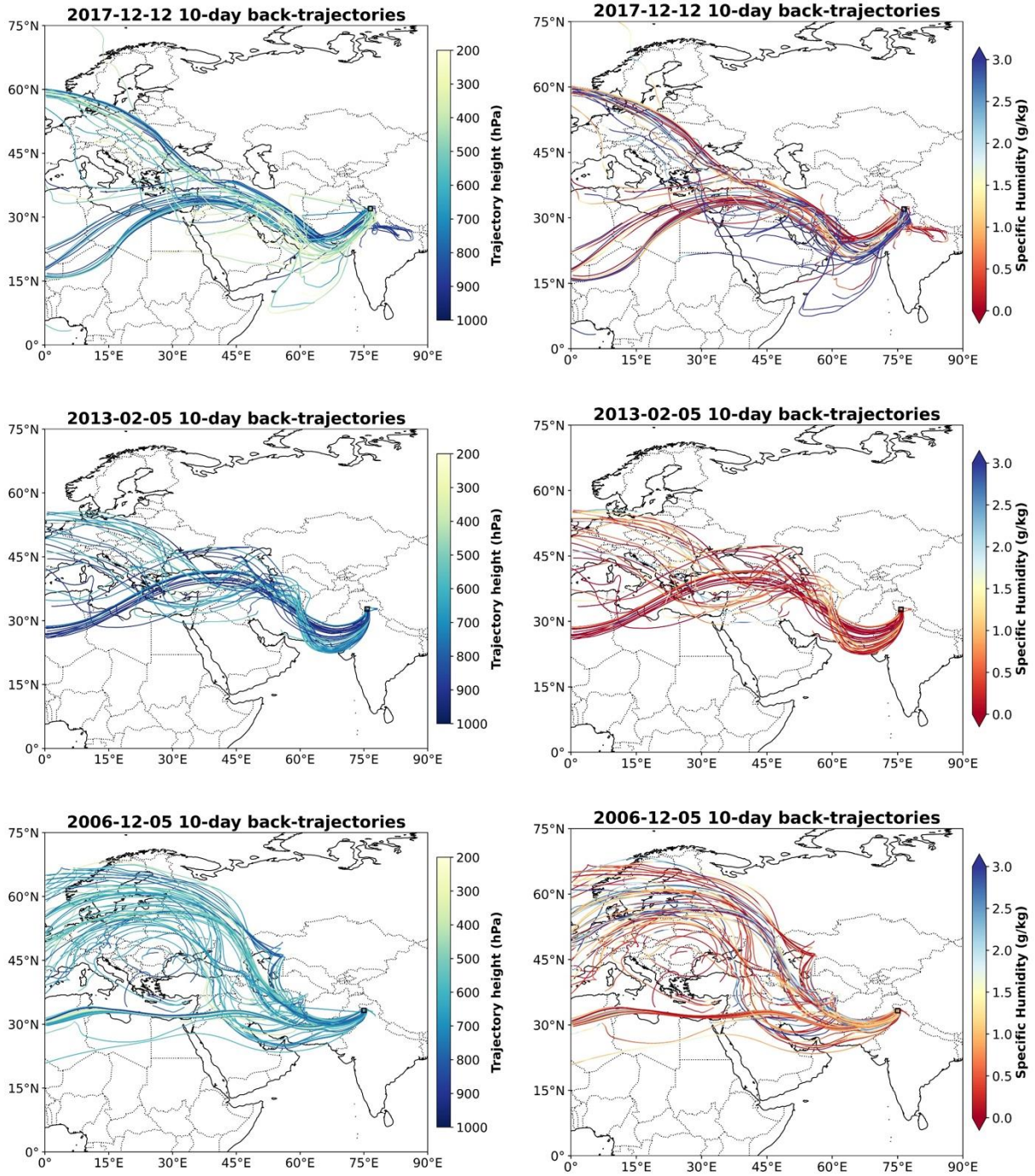

Figure 8: Forty parcels back trajectories (first column) initialized in atmospheric columns for selected winter EPEs, equally spaced between 925 and 500 hPa pressure levels. The trajectories are computed backward for 10 days according to the local and contemporaneous ERA-5 winds. Specific humidity corresponding to respective case studies have been provided in the right panel. The columns are located at (a) 32.25°N, 76.5°E (first row); (b) 32.75°N, 75.75°E (second row) and (c) 33.25°N, 74.75°E, (third row) for the extreme precipitation events on 12 December 2017, 05 February 2013 and 05 Dec 2006, respectively.

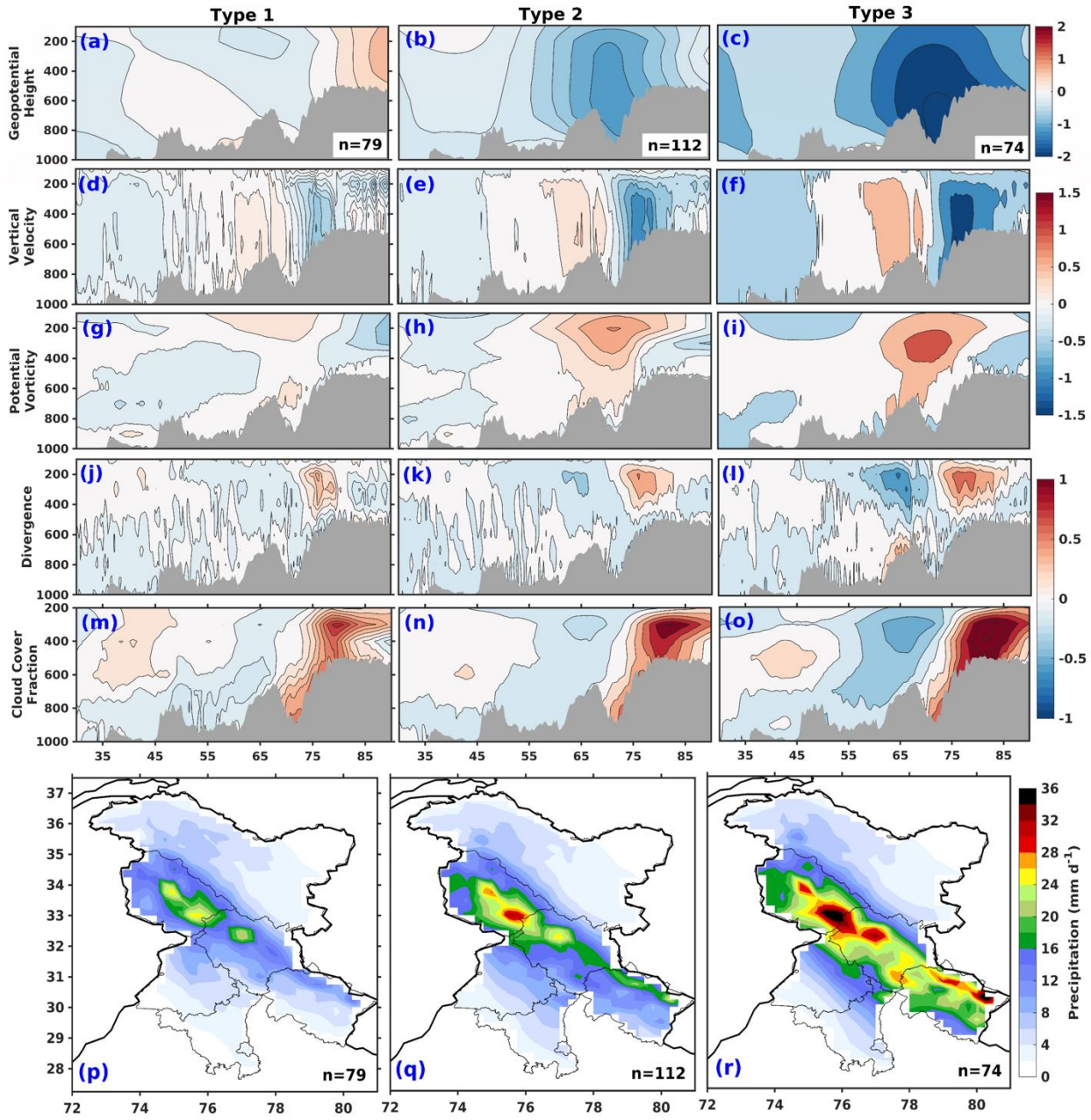

Figure 9: Classification of normalized anomalies of different dynamic and thermodynamic variables for precipitation extreme days (exceeding 95th percentile threshold) based on a three-partition k-means clustering algorithm (a-o) and corresponding classification of precipitation intensity during extremes (p-r) based on ERA5. Populations belonging to each cluster are given in respective panels.

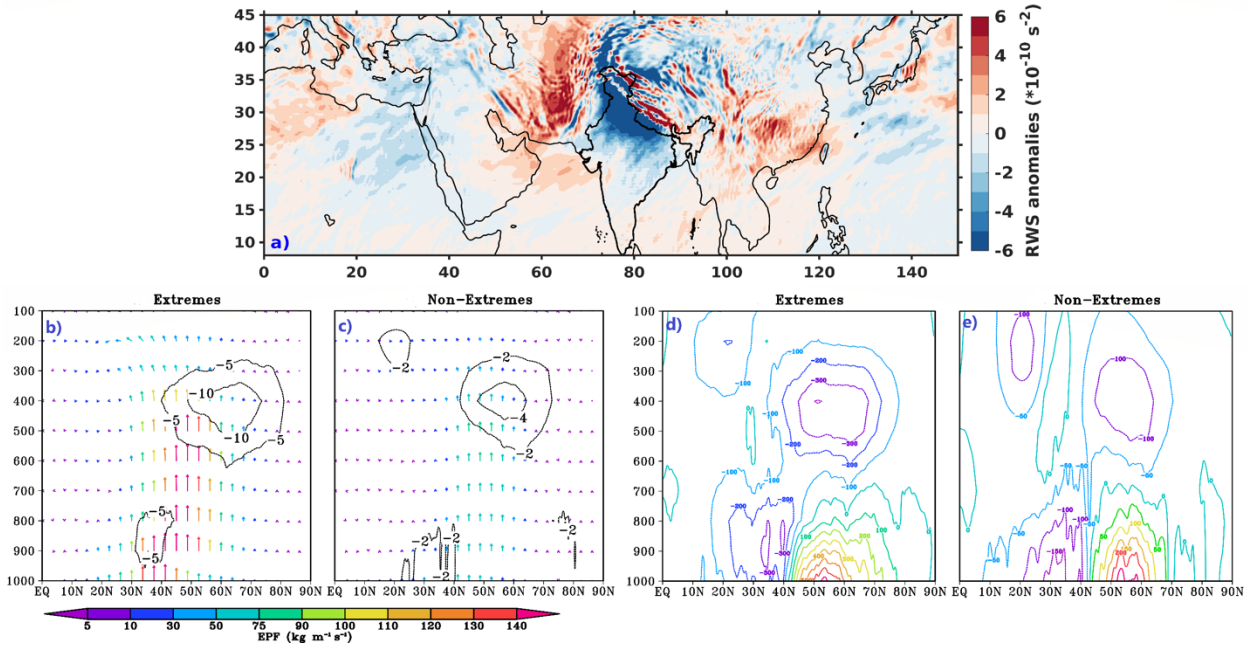

Figure 10: Winter composites (extremes minus non-extremes) for Rossby wave source anomalies (a; unit: s^{-2}) and, latitude-pressure cross-sections for zonally averaged Eliassen-Palm (EP) flux (b-c; vectors; unit: m^3s^{-1}), westerly wind acceleration (b-c; contours; unit: ms^{-2}) and, EP divergence (d-e; unit: ms^{-2}) in ERA5 during 1979-2019.

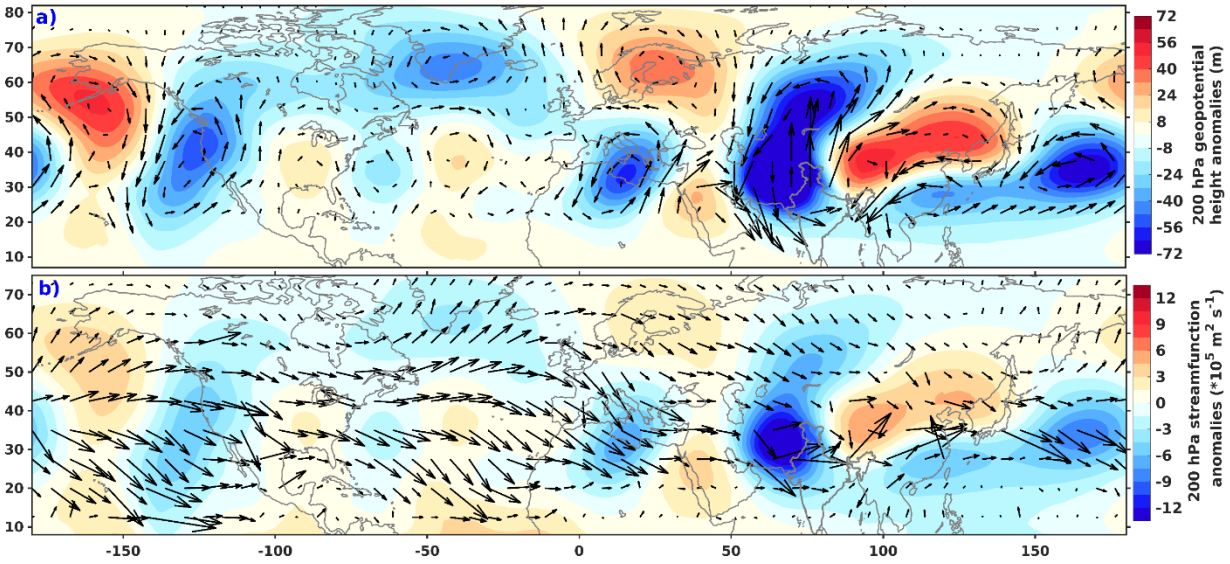

Figure 11: Spatial distribution of composited anomalies of upper-tropospheric (200 hPa) geopotential height (a; shaded; unit: m), wind vectors (a; unit: ms^{-1}), stream function (b; shaded; unit: m^2s^{-1}) and wave activity flux (b; unit: m^2s^{-2}) in ERA5 dataset during 1979-2019.

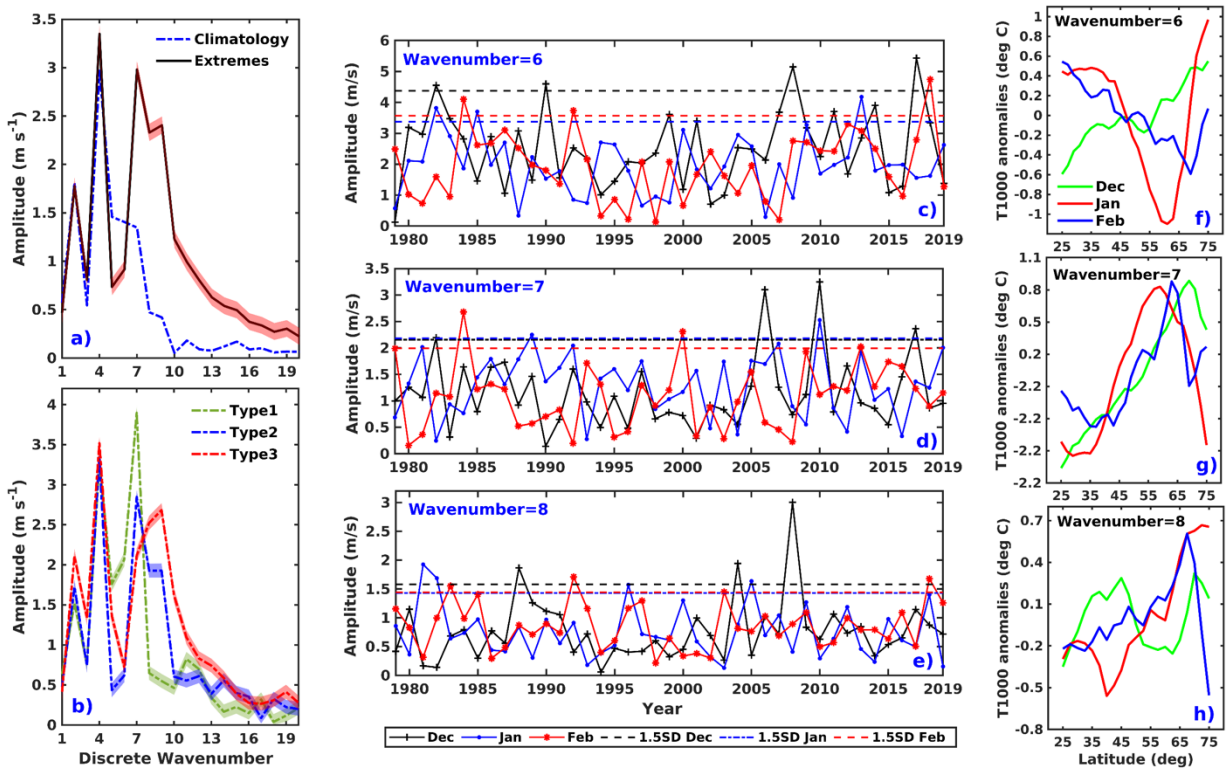

Figure 12: Zonal wave number spectra for the 300 hPa meridional wind averaged zonally over 30°-45°N for all identified precipitation extreme day composites in comparison to climatology (a) and; for extreme days composites associated with different clusters (b) in ERA5 dataset between 1979-2019. The filled area around the lines represents a 99% confidence interval. Interannual trends for the amplitudes of monthly mean Fourier components of the zonal wave spectra during DJF months associated with wave numbers 6/7/8. The dotted lines indicate 1.5SD amplitudes for different months (c-e). QRA fingerprint evaluated using 1000-hPa meridional temperature anomalies during DJF months associated with wave numbers 6/7/8 for the years identified from 1.5SD amplitudes in Fourier time series (f-h) and, zonally averaged 300 hPa zonal wind profiles for the same (i).

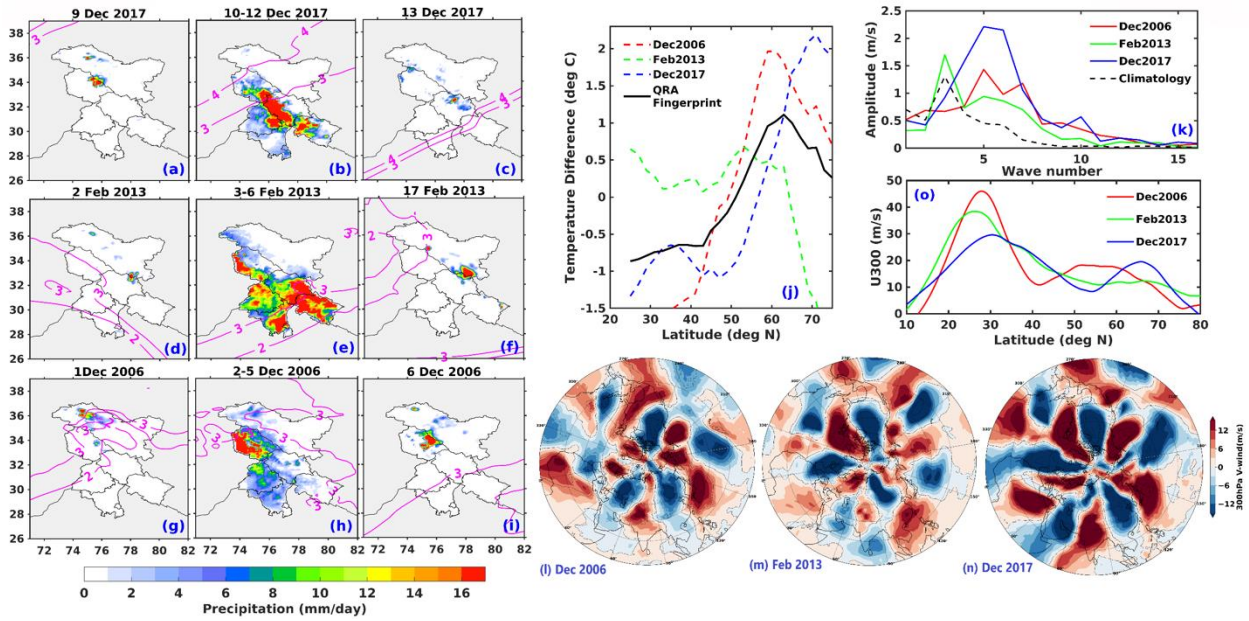

Figure 13: Spatial distribution of precipitation anomalies (shaded) before, during, and after the occurrence of precipitation extremes for individual case studies (10-12 December 2017(a-c), 3-6 February 2013 (d-f) and, 2-5 December 2006 (g-i)) from GPM-IMERG and, 300 hPa isentropic potential vorticity (a-i, contours; unit: PVU) for the events (before, during, and after) from ERA5. 1 PVU (potential vorticity units) here is equivalent to 10^{-6} $km^2/kg/s$. QRA fingerprint (j) evaluated using 1000 hPa meridional temperature anomalies for individual case studies and their composite (black line). Zonal wave number spectra for the 300 hPa meridional wind averaged zonally over 30°-45°N for all three events in comparison to climatology (k), composited 300 hPa meridional wind anomalies for the selected events (l-n) and, zonally averaged 300 hPa zonal wind profiles for the same (o).